J. Fluid Mech. (2006), *vol.* 547, *pp.* 65–104.
doi:10.1017/S0022112005007196 Printed in the United Kingdom

Investigation of the subgrid-scale stress and its production rate in a convective atmospheric boundary layer using measurement data

By QINGLIN CHEN AND CHENNING TONG†

Department of Mechanical Engineering, Clemson University, Clemson, SC 29634, USA

(Received 3 February 2005 and in revised form 7 July 2005)

The subgrid-scale (SGS) stress in the atmospheric surface layer is studied using measurement data. Field measurements employing a novel array technique were conducted to provide data for obtaining resolvable- and subgrid-scale variables. We analyse the conditional SGS stress and the conditional stress production rate conditional on the resolvable-scale velocity, which must be reproduced by the SGS model for large-eddy simulation (LES) to predict correctly the one-point resolvable-scale velocity statistics. The results show that both buoyancy and shear play important roles in the physics of the SGS stress. Strong buoyancy and vertical shear associated with updrafts and positive streamwise velocity fluctuations cause conditional forward energy transfer and strong anisotropy in the conditional SGS stress. Downward returning flows associated with large convective eddies result in conditional energy backscatter and much less anisotropic SGS stress. Predictions of the conditional SGS stress and the conditional stress production rate predicted using several SGS models are compared with measurements. None of those models are able to predict correctly the trends of both statistics. The Smagorinsky and one nonlinear model under-predict the anisotropy and the variations of the anisotropy, whereas the other nonlinear model and the mixed model over-predict both. The deficiencies of the SGS models that cause inaccurate LES statistics, such as the over-prediction of the mean shear and under-prediction of the vertical velocity skewness, are identified. The present study shows that analyses of conditional SGS stress and conditional SGS stress production provide a systematic approach for studying SGS physics and evaluating SGS models and can potentially be used to target specific aspects of LES that are important for a given application.

1. Introduction

Large-eddy simulation (LES) has become a very important approach for computing engineering and environmental turbulent flows (Lilly 1967; Deardorff 1970, 1972; Moeng & Wyngaard 1984; Nieuwstadt & de Valk 1987; Schmidt & Schumann 1989; Germano *et al.* 1991; Mason & Thomson 1992; Wyngaard 1992; Sullivan, McWilliams & Moeng 1994; Lesieur & Métais 1996; Meneveau & Katz 2000). LES computes the large, or resolvable scales of turbulent flows, and models the effects of the small, or subgrid (SGS) scales. When the filter scale is in the inertial range, as is often the case in the interior of a turbulent boundary layer or in the fully developed region of a free shear flow, the energy-containing scales are well resolved and most of the turbulent stress is carried by the resolvable scales. Under such conditions, the LES result is to some extent insensitive to the subgrid-scale model employed

† Author to whom correspondence should be addressed: ctong@ces.clemson.edu.

(Nieuwstadt & de Valk 1987; Mason 1994). The role of the subgrid scales is considered to be limited to extracting energy from the resolvable scales at the correct rate (Lilly 1967; Domaradzki, Liu & Brachet 1993; Borue & Orszag 1998).

However, in LES of high-Reynolds-number turbulent boundary layers, such as the atmospheric boundary layer (ABL), the filter scale in the near-wall region is inevitably in the energy-containing scales because the latter scale with the distance from the surface (Kaimal *et al.* 1972; Mason 1994; Peltier *et al.* 1996; Tong *et al.* 1998; Tong, Wyngaard & Brasseur 1999). Consequently, a significant portion of the turbulent stress must be carried by the SGS model, thereby causing strong dependence of the results on the SGS model (Tong *et al.* 1999). The deficiencies in the SGS model are therefore more likely to lead to errors in LES results in the near-wall region. For example, LES of the unstable ABL using the Smagorinsky model over-predicts the mean shear and the streamwise velocity variance (Nieuwstadt & de Valk 1987; Mason 1994; Sullivan *et al.* 1994; Khanna & Brasseur 1997) in the surface layer, and at the same time under-predicts the vertical velocity skewness. On the other hand, the standard dynamic Smagorinsky model, which generally performs better than the Smagorinsky model, under-predicts the mean shear (Porté-Agel, Meneveau & Parlange 2000). The under resolution and the strong dependence of the LES results on SGS models are an inherent problem in high-Reynolds-number boundary layers and cannot be solved by reducing the filter size (Mason 1994; Peltier *et al.* 1996; Tong *et al.* 1998, 1999).

These deficiencies in LES results have been argued to be related to the Smagorinsky model's being too dissipative (Mason 1994; Sullivan *et al.* 1994) and the dynamic model's being not dissipative enough (Porté-Agel *et al.* 2000). Various methods for improving LES results have been developed, including stochastic backscatter (Schumann 1975; Leith 1990; Mason & Thomson 1992), the split model of Schumann (Schumann 1975; Sullivan *et al.* 1994), a nonlinear model (Kosović 1997), and the scale-dependent dynamic Smagorinsky model (Porté-Agel *et al.* 2000). Mason & Thomson (1992) argued that the problem could be addressed by simply changing the length scale in the Smagorinsky model. They included a stochastic forcing term in the LES equation to represent the energy backscatter process, which was absent in the Smagorinsky model. Significant improvements in the mean velocity profile and the streamwise velocity variance profiles were achieved. Sullivan *et al.* (1994) modified the split model of Schumann (Schumann 1975), which consisted of an isotropic part and an anisotropic part for the model SGS stress. The latter is produced only by the mean shear strain rate. Such a formulation reduced the impact of the Smagorinsky model on the fluctuating fields and the energy dissipation, making the smallest resolved scales more energetic. Improvements similar to those obtained by Mason & Thomson (1992) were achieved. Kosović (1997) constructed a nonlinear model that includes both the strain rate and the rotation tensors based on the argument that the SGS stress is not frame indifferent. The model yielded an improved mean velocity profile, but also resulted in redistribution of the energy among the normal SGS stress components. Porté-Agel *et al.* (2000) argued that in the surface layer the coefficients in the dynamic Smagorinsky model were not equal at the LES and test filters. They used a second test filter and an assumption of power-law variations to account for this scale dependence. The results for the mean velocity profile, velocity variance profiles, and the velocity spectra showed improvements over the standard dynamic model. The improvements achieved by these methods demonstrated the importance of incorporating surface-layer SGS physics into SGS models and of systematically understanding the effects of model behaviours on LES results.

Traditionally, SGS models are studied primarily in two ways: *a priori* and *a posteriori* tests (e.g. Clark, Ferziger & Reynolds 1979; McMillan & Ferziger 1979; Bardina, Ferziger & Reynolds 1980; Nieuwstadt & de Valk 1987; Piomelli, Moin & Ferziger 1988; Lund & Novikov 1992; Mason & Thomson 1992; Domaradzki *et al.* 1993; Piomelli 1993; Härtel *et al.* 1994, Liu, Meneveau & Katz 1994; Mason 1994; Meneveau 1994; Peltier *et al.* 1996; Juneja & Brasseur 1999; Sarghini, Piomelli & Balaras 1999; Tao, Katz & Meneveau 2000; Porté-Agel *et al.* 2001; Sullivan *et al.* 2003). Traditional tests have contributed greatly to our understanding of the current SGS models. However, they also have their limitations. For *a priori* tests, it is difficult to predict the effects of model behaviours on LES results. For example, the correlation between the modelled and measured SGS stress components provides little information about model performance in a simulation. For *a posteriori* tests, it is difficult to relate deficiencies of LES results to specific aspects of the model behaviours. This is not only because the SGS stress evolves LES fields through dynamic equations, but also because the equations are chaotic with many degrees of freedom, making it difficult to relate the properties of the solutions to the behaviours of the SGS terms in the equation.

In view of the difficulties in directly assessing the model effects on LES results, it is important to use a more systematic approach for analysing SGS models. While SGS models affect the predicted instantaneous flow fields and structures, their impact on flow statistics is arguably the most important and should first be understood. In fact, Pope (2000) argues that the best LES that can be achieved is one that statistically corresponds to the true resolvable-scale fields. Although it is not practical to expect an SGS model to predict all the statistics of the resolvable-scale fields, it should at least be able to predict those important for specific applications (e.g. mean and r.m.s. profile, spectra, vertical velocity skewness, etc.). Because flow statistics are often strongly influenced by flow structures, their correct predictions will also benefit the predicted flow structures. Therefore, an important task in improving an SGS stress model is to understand how the SGS stress affects the resolvable-scale velocity statistics.

To this end, an analysis method relating the SGS model to LES statistics is needed. Dynamic equations for the statistics of the resolvable-scale velocity are a very useful choice. Pope (2000) and Langford & Moser (1999) have provided the necessary and sufficient conditions for LES to predict correctly all one-time multi-point joint probability density function (JPDF) of the resolvable-scale velocity: the conditional mean of the SGS stress conditional on the entire resolvable-scale velocity field must be reproduced by the modelled SGS stress. A model that satisfies this condition will yield the optimal LES. This condition is an extension of that given by Adrian (1990). However, in practice, it is not feasible to obtain this conditional SGS stress as it requires a large number of resolvable-scale velocity fields to cover the functional space. In the present work, we study the influence of the SGS motions on the resolvable-scale statistics by analysing the transport equation of the one-time one-point JPDF of the resolvable-scale velocity components.

The JPDF equation can be derived following the method given by Pope (1985) and Meneveau (1994) using the equation for the resolvable-scale velocity

$$\frac{\partial u_i^r}{\partial t} = -\frac{\partial u_j^r u_i^r}{\partial x_j} - \frac{\partial \tau_{ij}}{\partial x_j} - \frac{\partial p^r}{\partial x_i} + \frac{g}{\Theta}\theta^r \delta_{i3} + \nu \frac{\partial^2 u_i^r}{\partial x_j \partial x_j}, \tag{1.1}$$

where

$$\tau_{ij} = (u_i u_j)^r - u_i^r u_j^r$$

is the SGS stress (the Leonard stress $L_{ij} = (u_i^r u_j^r)^r - u_i^r u_j^r$ has been included in τ_{ij}), a superscript r denotes a resolvable-scale variable, and Θ and θ are the mean and fluctuation potential temperatures, respectively. Taking the time derivative of the JPDF, $f = \langle f' \rangle = \langle \prod_{i=1}^{3} \delta(u_i^r - v_i) \rangle$, where f' is the fine-grained JPDF and the angle brackets denote an ensemble mean, we obtain

$$\frac{\partial f}{\partial t} = \left\langle \frac{\partial f'}{\partial u_i^r} \frac{\partial u_i^r}{\partial t} \right\rangle = -\frac{\partial}{\partial v_i} \left\langle \frac{\partial u_i^r}{\partial t} f' \right\rangle. \tag{1.2}$$

Substituting $\partial u_i^r / \partial t$ in the right-hand side of (1.2) leads to the JPDF equation

$$\begin{aligned} \frac{\partial f}{\partial t} + v_j \frac{\partial f}{\partial x_j} = {} & \frac{\partial}{\partial v_i} \left\{ \left\langle \frac{\partial \tau_{ij}}{\partial x_j} \middle| \boldsymbol{u}^r = \boldsymbol{v} \right\rangle f \right\} \\ & + \frac{\partial}{\partial v_i} \left\{ \left\langle \frac{\partial p^r}{\partial x_i} \middle| \boldsymbol{u}^r = \boldsymbol{v} \right\rangle f \right\} - \frac{g}{\Theta} \frac{\partial}{\partial v_3} \{ \langle \theta^r | \boldsymbol{u}^r = \boldsymbol{v} \rangle f \}. \end{aligned} \tag{1.3}$$

The left-hand side of the equation is the time derivative and the advection in physical space. The right-hand side is transport in velocity space of the JPDF by the SGS stress divergence, the resolvable-scale pressure gradient, and the buoyancy force. Transport due to viscous force is generally small at high Reynolds numbers and is omitted from the equation. Galilean invariance of the velocity JPDF equation has been proved (Tong 2003).

An alternative form of the equation was given by Chen *et al.* (2003)

$$\begin{aligned} \frac{\partial f}{\partial t} + v_j \frac{\partial f}{\partial x_j} = {} & \frac{\partial^2}{\partial v_i \partial x_j} \{ \langle \tau_{ij} | \boldsymbol{u}^r = \boldsymbol{v} \rangle f \} + \frac{\partial^2}{\partial v_i \partial v_j} \left\{ \left\langle -\tfrac{1}{2} P_{ij} \middle| \boldsymbol{u}^r = \boldsymbol{v} \right\rangle f \right\} \\ & + \frac{\partial^2}{\partial v_i \partial x_i} \{ \langle p^r | \boldsymbol{u}^r = \boldsymbol{v} \rangle f \} + \frac{\partial^2}{\partial v_i \partial v_j} \left\{ \left\langle p^r \frac{\partial u_j^r}{\partial x_i} \middle| \boldsymbol{u}^r = \boldsymbol{v} \right\rangle f \right\} \\ & - \frac{g}{\Theta} \frac{\partial}{\partial v_3} \{ \langle \theta^r | \boldsymbol{u}^r = \boldsymbol{v} \rangle f \}. \end{aligned} \tag{1.4}$$

The right-hand side now represents mixed transport in physical and velocity spaces by the conditional SGS stress and the resolvable-scale pressure and transport in velocity space by the conditional SGS stress production rate, $\langle -(1/2) P_{ij} | \boldsymbol{u}^r = \boldsymbol{v} \rangle$, the conditional resolvable-scale pressure–strain correlation, and the conditional buoyancy force, where

$$P_{ij} = -\left\{ \tau_{ik} \frac{\partial u_j^r}{\partial x_k} + \tau_{jk} \frac{\partial u_i^r}{\partial x_k} \right\}. \tag{1.5}$$

Equation (1.4) shows that the SGS stress directly affects the resolvable-scale velocity JPDF through the conditional SGS stress and the conditional SGS stress production and indirectly through the pressure terms. Therefore, the necessary conditions for LES to correctly predict the velocity JPDF are that the conditional means of SGS stress and SGS stress production rate must be reproduced by the SGS model (Chen *et al.* 2003). The conditions show that the modelled and true SGS stress should be compared statistically, not instantaneously, because a modelled SGS stress field can satisfy these conditions, yet does not correlate well with the true SGS stress. We note that although in LES we solve equation (1.1), the SGS model evolves the JPDF according to equation (1.3) or (1.4).

Equation (1.4) provides a link between the SGS stress and the resolvable-scale velocity JPDF and can be used to study the effects of the SGS stress on the JPDF. It

also reveals two important effects of the SGS turbulence on the resolvable scales. First, the trace of $\langle P_{ij}|\boldsymbol{u}^r = \boldsymbol{v}\rangle$ is the conditional energy transfer rate from the resolvable to the subgrid scales. Therefore, equation (1.4) provides an analytical proof that the (conditional) energy transfer is essential for the evolution of the JPDF (Chen *et al.* 2003), while previous studies have only argued its importance based on its role in the inertial-range turbulence. In addition, conditional forward transfer and conditional backscatter have qualitatively different effects on the evolution of the JPDF because the conditional energy transfer in (1.4) plays a role similar to the diffusion coefficient in a diffusion equation. Second, previous studies focused primarily on the SGS stress whereas equation (1.4) also points to the importance of the SGS stress production rate. Because the SGS stress and the SGS stress production are important for the SGS dynamics and have clear physical meanings; their results can be interpreted better than those for the SGS stress divergence in (1.3).

In the present study, we investigate the necessary conditions for LES to reproduce the JPDF and the dependences of the terms in the JPDF equation on the surface layer dynamics to gain an understanding of the SGS physics that are important for SGS modelling and to examine SGS models. Although analyses of the terms in the JPDF equation using experimental data are still *a priori* in nature, they differ qualitatively from previous *a priori* analyses in several aspects. First, the JPDF-based analyses deal with the conditional averages of the SGS stress and its production rate, which evolve the JPDF. Consequently, there exists a close link between the conditional statistics and the JPDF in the present analyses. On the other hand, the traditional model tests often compute the correlation coefficient between the modelled and true SGS stress, which generally cannot be related to LES statistics because the correlation in general cannot be used to measure the model performance for predicting the conditional SGS stress (and more so for the conditional SGS stress production rate). Second, the system described by the JPDF equation is not chaotic. The solution of the JPDF equation is a statistic (a deterministic field) and is generally stable to small perturbations in initial and boundary conditions as well as the modelled terms. Therefore, an SGS model that provides close approximations of the conditional SGS stress and the conditional SGS stress production is consistent with the above mentioned necessary conditions, thereby having the potential to predict the JPDF well and vice versa. Such *a priori* analyses are in contrast with the traditional tests: because the LES equation (1.1) is chaotic, i.e. its solution exhibits stochastic behaviours, any imperfection in the correlation between the modelled and true SGS stress will cause the LES field to diverge exponentially from the true resolvable-scale field, making it practically impossible to relate the modelled instantaneous SGS stress to LES results. Third, for the analyses based on the JPDF equation there are analytical results (e.g. Jaberi, Miller & Givi 1996; Sabelnikov 1998) that can be used as a basis to investigate the relationship between the SGS terms and the JPDF whereas no such analyses can be performed for the LES equation. Therefore, *a priori* tests based on the JPDF equation are fundamentally different from the traditional *a priori* tests and JPDF equations of the resolvable-scale velocity provide a more rational approach for studying the effects of the SGS stress and SGS models on the resolvable-scale statistics.

In LES employing certain SGS models, such as the Smagorinsky model, only the deviatoric part of the SGS stress, $\tau_{ij}^d = \tau_{ij} - \tau_{kk}\delta_{ij}/3$, is modelled. Therefore, it is also useful to examine the corresponding production term P_{ij}^d defined as

$$P_{ij}^d = -\left\{\tau_{ik}^d \frac{\partial u_j^r}{\partial x_k} + \tau_{jk}^d \frac{\partial u_i^r}{\partial x_k}\right\}. \tag{1.6}$$

Thus, P_{ij} can be written as

$$P_{ij} = P_{ij}^d - \tfrac{2}{3}\tau_{kk}S_{ij}, \tag{1.7}$$

where S_{ij} is the resolvable-scale strain rate tensor. Equation (1.6) shows that P_{ij}^d is the production rate due to the interaction between the deviatoric (anisotropic) part of the SGS stress and the resolvable-scale velocity gradient, and $-2\tau_{kk}S_{ij}/3$ is the production rate due to straining of the isotropic part of the SGS stress by the resolvable-scale strain rate. Therefore, the normal components of P_{ij} contain the energy transfer from the resolvable to the subgrid scales, $P_{\alpha\alpha}^d$ ($\alpha = 1, 2, 3$), and the redistribution among three normal components of the SGS stress (inter-component exchange), $-2\tau_{kk}S_{\alpha\alpha}/3$, respectively. Note that the summation of inter-component exchange $-2\tau_{kk}S_{ll}/3$ is zero, indicating that this term redistributes energy among the three normal components of the SGS stress. Therefore, the anisotropy of the normal SGS stress components is important for the evolution of the JPDF. The shear components of P_{ij}^d represent the production of SGS shear stress in anisotropic turbulence due to both straining and rotation by the resolvable-scale velocity field. The shear components $-2\tau_{kk}S_{ij}/3$ ($i \neq j$), represent the production of shear stress due to straining of isotropic SGS turbulence. Therefore the decomposition in (1.7) is useful for further understanding the physics of P_{ij}.

The dynamics of the SGS stress can also be examined using the SGS stress transport equation

$$\begin{aligned}\frac{\partial \tau_{ij}}{\partial t} + u_k^r \frac{\partial \tau_{ij}}{\partial x_k} = {} & \frac{\partial}{\partial x_k}\left\{u_k^r (u_i u_j)^r - (u_i u_j u_k)^r + \left(\tau_{ik}u_j^r + \tau_{jk}u_i^r\right)\right\} + P_{ij} + P_{Bij} \\ & - \left(u_j \frac{\partial p}{\partial x_i}\right)^r - \left(u_i \frac{\partial p}{\partial x_j}\right)^r + u_i^r \frac{\partial p^r}{\partial x_j} + u_j^r \frac{\partial p^r}{\partial x_i} - \epsilon_{ij}.\end{aligned} \tag{1.8}$$

The left-hand side is the time rate of change and advection. The right-hand side is the turbulent transport, turbulent production, buoyancy production, pressure transport and destruction and molecular dissipation ($2\nu(\partial u_i/\partial x_k)(\partial u_j/\partial x_k)$). The buoyancy production rate,

$$P_{Bij} = \frac{g}{\Theta}\left\{\delta_{i3}\left[(\theta u_j)^r - \theta^r u_j^r\right] + \delta_{j3}\left[(\theta u_i)^r - \theta^r u_i^r\right]\right\}, \tag{1.9}$$

has only three non-zero components P_{Bi3}; therefore, it affects only the τ_{i3} components. Wyngaard, Coté & Izumi (1971) showed that the shear production of the Reynolds shear stress exceeds that of energy under all stability conditions, whereas the buoyancy production of shear stress is larger than that of energy under neutral and stable conditions, but falls off as the surface layer becomes more unstable. These results suggest that the magnitude of shear to buoyancy production of the SGS stress is also important for the behaviour of the SGS stress.

Pope (2004) discussed the issue of LES statistics and argued that the perfect LES should correctly predict all statistics of the total velocity, not those of the resolvable-scale velocity. He showed that the dynamic Smagorinsky model, in fact, minimized the dependence of the predicted total stress on the filter scale, thereby improving the predictions when the filter scale is larger than the inertial-range scales. While the perfect LES is desirable, in many cases, the SGS model has no direct contribution to the higher-order statistics of the total velocity. For example, an SGS stress model only contributes to the vertical velocity skewness through its correlation with the resolvable-scale vertical velocity, while the contribution from the SGS vertical velocity is not predicted. More generally, the one-point PDF of the total velocity cannot be estimated using models for SGS stress. To predict the total velocity PDF, a different

approach that models the SGS velocity distribution is required, e.g. the filtered density function methods (Gicquel *et al.* 2002; Wang, Tong & Pope 2004). Therefore, for LES employing SGS stress models, the optimal LES can only be expected to reproduce the true resolvable-scale statistics, which approach the total velocity statistics as the filter scale is asymptotically small compared to the energy-containing scales.

In the present study, the subgrid-scale (SGS) stress and its production rate in the unstable atmospheric surface layer are studied using field measurements data. The rest of the paper is organized as follows. Section 2 outlines the field program and the array filter technique for measuring resolvable- and subgrid-scale variables. The measured conditional SGS stress and the conditional SGS stress production are discussed in § 3. Sections 4 and 5 present the SGS model predictions and their implications for SGS modelling. Some further discussions on the relationships between the conditional SGS stress and the conditional SGS stress production are given in § 6, followed by the conclusions.

2. Field measurements and data analysis procedures

The field measurements for this study, named the horizontal array turbulence study, or HATS field program, were conducted at a field site 5.6 km east-northeast of Kettleman City, California, in the summer of 2000 as a collaboration primarily among the National Center for Atmospheric Research, Johns Hopkins University and Penn State University (CT was part of the Penn State group). Horst *et al.* (2004) describe the field site and the data collection procedures in detail.

The field measurement design is based on the transverse array technique proposed, studied, and first used by the Penn State group (Edsall *et al.* 1995; Tong *et al.* 1997, 1998, 1999) for surface-layer measurements in the ABL. It has subsequently been used by several groups in the ABL over land (Tong *et al.* 1997, 1999; Porté-Agel *et al.* 2001; Kleissl, Meneveau & Parlange 2003; Horst *et al.* 2004) and ocean (the recent ocean HATS program) as well as in engineering flows (Cerutti, Meneveau & Knio 2000; Tong 2001; Wang & Tong 2002; Rajagopalan & Tong 2003; Chen *et al.* 2003; Wang *et al.* 2004). The technique uses horizontal sensor arrays (figure 1) to perform two-dimensional filtering to obtain resolvable- and subgrid-scale variables. Two arrays are vertically spaced to obtain vertical derivatives. The primary horizontal array consists of nine equally spaced sonic anemometers (Campbell Scientific SAT3) and the secondary array has five sonics at a second height. The arrays are aligned perpendicularly to the prevailing wind direction.

The filter operation in the streamwise direction is performed by invoking Taylor's hypothesis. Filtering in the transverse direction is realized by averaging the output of the signals from the sensor array (Tong *et al.* 1998). For example, the transversely filtered resolvable-scale velocity (denoted by a superscript t) is obtained as

$$u_i^t(\boldsymbol{x}, t) = \sum_{j=-N}^{N} C_j u_i(x_1, x_2 + j \times d, x_3, t), \tag{2.1}$$

where $2N+1$, C_j and d are the number of sensors on an array, the weighting coefficient for the jth sensor and the spacing between adjacent sensors, respectively. We use $2N + 1 = 5$ and 3 for filtering at the heights of the primary and secondary arrays, respectively, to maintain the same filter size. The subgrid-scale velocity is obtained by subtracting the resolvable-scale part from the total velocity. In the present study, we use the arrays to approximate top-hat filters, which are the most compact type

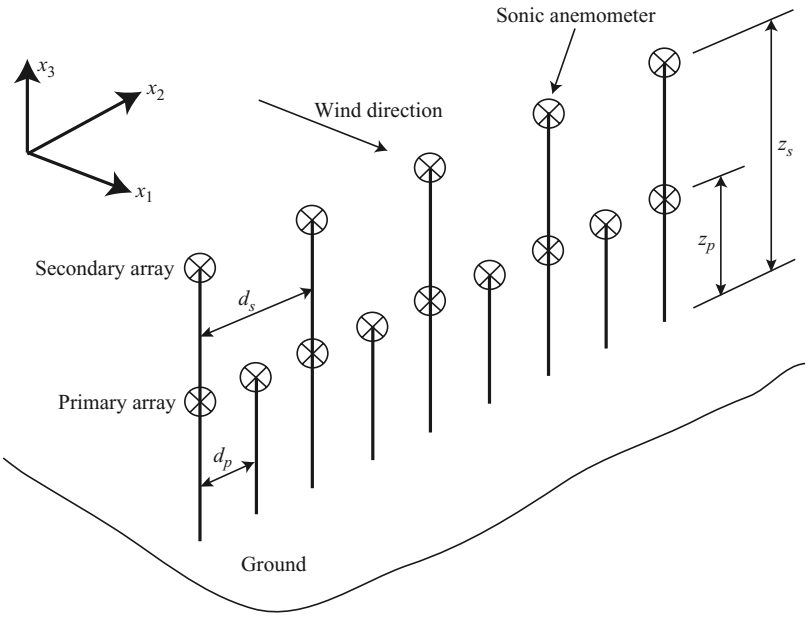

FIGURE 1. Schematic of the array set-up. The secondary array (denoted by a subscript s) is used to obtain derivatives in the vertical direction.

in physical space. Because derivatives are computed using finite differencing (with a spacing of $4d_p$ in the horizontal directions), which is effectively a top-hat filter, top-hat filters provide consistency among the resolvable-scale velocity and its derivatives.

The issues in applying the array filtering technique, including the accuracy of the array filter and the use of Taylor's hypothesis, have been systematically studied by Tong *et al.* (1998). They showed that a two-dimensional filter is a good approximation of a three-dimensional filter. They demonstrated that among the mechanisms that could affect the accuracy of Taylor's hypothesis (Lumley 1965), including the effect of different convection velocity for different wavenumber components, temporal changes in the reference moving with the mean velocity, and the fluctuating convecting velocity, only the last one is significant. Their analyses of the accuracy of a spectral cutoff array filter as an approximation of a true two-dimensional filter showed that the r.m.s. values of the filtered variables differ by less than 10 %. Because the spectral cutoff filter has the slowest decay in physical space, it is the most difficult to approximate by the array. Therefore, the accuracy of the top-hat filter array filter is expected to be higher. The error associated with one-side finite differencing in the vertical direction is examined by Kleissl *et al.* (2003). They evaluated the divergence-free condition for the filter velocity field and concluded that reasonable accuracy can be achieved in computing derivatives of filtered velocity. Horst *et al.* (2004) further studied various issues of using the array technique including the aliasing errors associated with evaluating derivatives using finite diffferencing and also demonstrated sufficient accuracy of the technique.

Four different array configurations, shown in table 1, are employed in the HATS program. The filter (grid) aspect ratio (Δ/z) ranges from 0.48 to 3.88, allowing the effects of grid anisotropy to be examined. We refer to z as the height of the primary array z_p here and hereinafter. Array 3 is at a much higher z, therefore the effects of the stability parameter $-z/L$ can be examined, where $L = -u_*^3\Theta/k_a g\langle u_3'\theta'\rangle$, $u_*^2 = -\langle u_1'u_3'\rangle$

Array	Δ/z_p	z_p	d_p	z_s	d_s
1	3.88	3.45	3.35	6.90	6.70
2	2.00	4.33	2.167	8.66	4.33
3	1.00	8.66	2.167	4.33	1.08
4	0.48	4.15	0.50	5.15	0.625

TABLE 1. Configurations of the four arrays (lengths in metres).

Data	$\langle u \rangle$ ($\mathrm{m\,s^{-1}}$)	$-z/L$	u_* ($\mathrm{m\,s^{-1}}$)	ϵ ($\mathrm{m^2\,s^{-3}}$)	H ($\mathrm{K\,m\,s^{-1}}$)	Duration (min)
a	1.42	0.34	0.15	0.003	0.02	35
b	3.56	0.22	0.33	0.031	0.17	30
c	3.65	0.21	0.36	0.039	0.20	83
d	3.25	0.24	0.36	0.041	0.24	33

TABLE 2. Surface-layer parameters for array 1 ($\Delta/z = 3.88$) under unstable conditions. The primary array height z_p is used for z.

Array	Δ/z ($\approx$)	$\langle u \rangle$ ($\mathrm{m\,s^{-1}}$)	$-z/L$	u_* ($\mathrm{m\,s^{-1}}$)	ϵ ($\mathrm{m^2\,s^{-3}}$)	Total duration (min)
2	2.00	3.09	0.36	0.30	0.020	257
3	1.00	4.22	0.60	0.34	0.018	591
4	0.48	2.73	0.35	0.30	0.021	60

TABLE 3. Surface-layer parameters for the other arrays under unstable conditions. The primary array height z_p is used for z.

(a prime denotes fluctuations), $k_a = 0.41$ and g are the Monin–Obukov length, friction velocity, von Kármán constant and acceleration due to gravity, respectively. The surface layer parameters for the data sets collected using the four arrays are given in tables 2 and 3. The results in § 3.3 show that the SGS stress for array 1, which has the largest Δ/z, is the most anisotropic and most difficult for SGS models to predict, therefore our discussions of results focus on array 1. All array 1 data used in the present study were collected during daytime under clear conditions and the boundary layer was convective with a Monin–Obukov length of approximately -15 m.

Although the arrays were arranged to be perpendicular to the prevailing wind direction, the mean wind direction for a given data section might not be exactly perpendicular to the array. Therefore, we rotate the coordinate system and interpolate the velocity and temperature in the Cartesian coordinate system defined by mean wind and cross-wind directions (Horst *et al.* 2004). The interpolation is performed in spectral space to avoid attenuating the high-frequency (wavenumber) fluctuations.

In the present work, we study the unstable surface layer, i.e. $z/L < 0$. Data sections that are quasi-stationary are generally 30–90 min in length. In order to achieve reasonable statistical convergence in our analysis, we combine the results of selected data sections collected under similar stability conditions using each array configuration. We focus on four data sections collected using array 1 (table 2). The conditional statistics obtained using the individual data sets (not shown) are very similar, but with varying degrees of uncertainty. Therefore, we normalize the results for each data set using its parameters, then weight-average them according to the number of conditional samples in each bin.

Array	σ_u^2/u_*^2	σ_v^2/u_*^2	σ_w^2/u_*^2	$\langle\tau_{11}\rangle/\sigma_u^2$	$\langle\tau_{22}\rangle/\sigma_v^2$	$\langle\tau_{33}\rangle/\sigma_w^2$	$\langle-\tau_{13}\rangle/u_*^2$
1	8.17	9.55	1.52	0.35	0.21	0.89	0.73
2	12.12	13.19	1.86	0.20	0.14	0.76	0.57
3	9.53	13.58	2.19	0.17	0.09	0.54	0.34
4	10.98	10.57	1.69	0.07	0.06	0.35	0.11

TABLE 4. Measured Reynolds stress and mean SGS stress for the four arrays.

Because of the complexity of the variables of interest and of the conditional sampling procedure, we are not able to provide a precise level of statistical uncertainty. However, by monitoring the statistical scatter while increasing the data size, we conclude that reasonable statistical convergence is achieved. An example of the convergence process is given in figure 3. In addition, comparisons between model predictions and measurements require only the relative magnitude of the results and are less affected by the uncertainty. Therefore, the data size is sufficient for obtaining reliable statistics for the analyses.

3. Results

In this section, we focus our discussions on results obtained using data from array 1. The stability parameter $-z/L$ has an average value of 0.24. Therefore, we expect both buoyancy and shear to affect the surface-layer turbulence. Top-hat filters in both streamwise and cross-stream directions are used to obtain the resolvable-scale and subgrid-scale variables with a filter size $\Delta = 3.88z$, which is in the energy-containing range. The results for the other array configurations, i.e. different Δ/z, and $-z/L$ (table 3), are also obtained. The results are generally similar to those for array 1. Therefore, we only briefly discuss their differences with those of array 1 and the influence of Δ/z and $-z/L$. Table 4 gives the normalized Reynolds stress and the ratios of the mean SGS stress components to the Reynolds stress components. Array 1 has the highest fraction of the vertical shear stress carried by the subgrid scales. The deviatoric part of the measured and modelled SGS stress components are given in table 5 and discussed in § 4.

The results for conditional SGS stress $\langle\tau_{ij}|\boldsymbol{u}^r\rangle$ are normalized by the friction velocity u_*^2. The results for the conditional SGS stress production $\langle P_{ij}|\boldsymbol{u}^r\rangle$, the buoyancy production $\langle P_{Bij}|\boldsymbol{u}^r\rangle$ and the advection term $\langle -u_3^r\partial\tau_{ij}/\partial x_3|\boldsymbol{u}^r\rangle$ are normalized by the estimated energy dissipation rate $\epsilon = \phi_\epsilon u_*^3/k_a z$, where $\phi_\epsilon = 1 - z/L$ for $z/L \leqslant 0$ as suggested by Kaimal *et al.* (1972).

3.1. *Normal components of* $\langle\tau_{ij}|\boldsymbol{u}^r\rangle$ *and* $\langle P_{ij}|\boldsymbol{u}^r\rangle$

The results for the conditional normal SGS stress components are plotted against the horizontal resolvable-scale velocity, u_1^r, for different values of the vertical resolvable-scale velocity, u_3^r (figure 2). Owing to the limited data size, we are not able to include the third velocity component in the conditional SGS stress. The data bin for the first conditioning variable (e.g. u_1^r in figure 2*a*) have the width shown in the figures (12 bins between ± 2 standard deviations whereas that for the second conditioning variable is twice as wide). Figure 3 gives a representative case (τ_{11}) of the convergence of the conditional SGS stress as the sample size is increased from one fifth to the full data set. Based on such tests, we conclude that reasonable statistical convergence is achieved. Figures 2(*a*) and 2(*c*) show that $\langle\tau_{11}|u_1^r, u_3^r\rangle$ and $\langle\tau_{33}|u_1^r, u_3^r\rangle$ generally increase

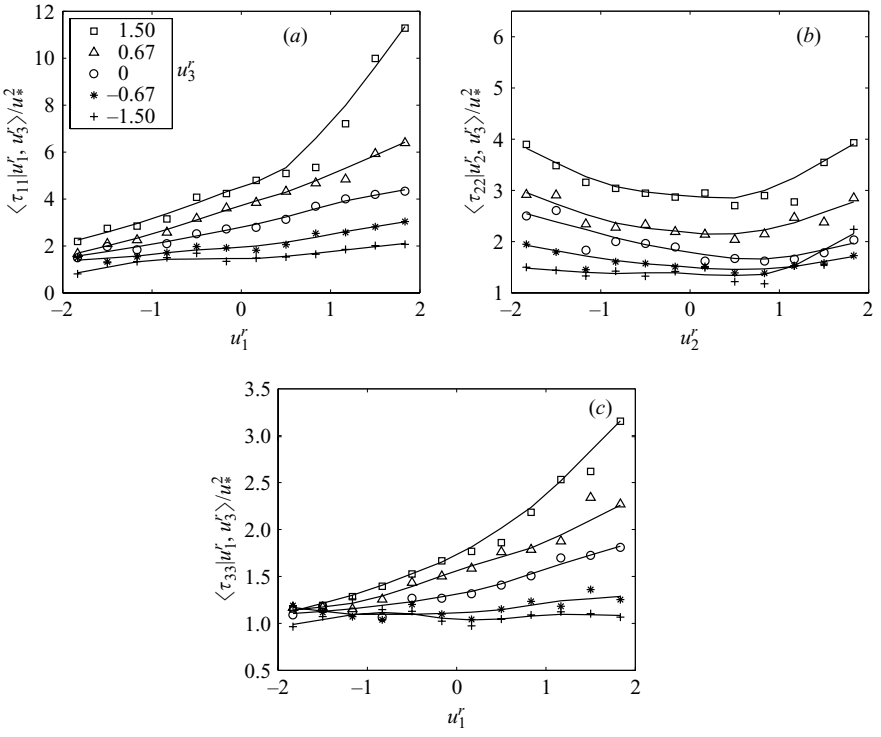

FIGURE 2. Conditional means of the measured normal SGS stress components conditional on the resolvable-scale velocity components. The dependence on the horizontal velocity components is stronger for positive u_3^r. Here and hereinafter u_i^r is normalized by the r.m.s. fluctuations of the total velocity σ_{u_i}.

with u_3^r. They also increase with u_1^r when u_3^r is positive, and depend weakly on u_1^r when u_3^r is negative, indicating that the dependence on u_1^r is enhanced by positive u_3^r. Figure 2(*b*) shows that $\langle \tau_{22}|u_2^r, u_3^r\rangle$ increases with u_3^r and $|u_2^r|$, but its dependence on $|u_2^r|$ is generally weaker than that of $\langle \tau_{11}|u_1^r, u_3^r\rangle$ on u_1^r. The dependence of $\langle \tau_{11}|u_1^r, u_3^r\rangle$ (and $\langle \tau_{22}|u_2^r, u_3^r\rangle$) on u_3^r can be attributed partly to the vertical advection (Tong *et al.* 1999). The measured advection (not shown) is generally positive for positive u_3^r and vice versa. This is because in the surface layer, the velocity variance varies slowly with the distance from the ground, whereas the length scale is proportional to the distance; therefore, the SGS eddies brought up from near the ground generally contain a larger magnitude of SGS stress.

The anisotropic part of the conditional SGS stress, $\langle \tau_{ij}^d|\boldsymbol{u}^r\rangle$, which is predicted by some SGS stress models, is also computed. The diagonal components $\langle \tau_{\alpha\alpha}^d|\boldsymbol{u}^r\rangle$ (no summation) are shown in figure 4. The off-diagonal components of $\langle \tau_{ij}^d|\boldsymbol{u}^r\rangle$ are identical to those of $\langle \tau_{ij}|\boldsymbol{u}^r\rangle$. The trends of $\langle \tau_{\alpha\alpha}^d|\boldsymbol{u}^r\rangle$ are similar to those in figure 2. The magnitudes of $\langle \tau_{11}^d|u_1^r, u_3^r\rangle$ and $\langle \tau_{22}^d|u_2^r, u_3^r\rangle$ become smaller compared to $\langle \tau_{11}|u_1^r, u_3^r\rangle$ and $\langle \tau_{22}|u_2^r, u_3^r\rangle$, and $\langle \tau_{33}^d|u_1^r, u_3^r\rangle$ becomes negative owing to the strong anisotropy of the surface layer ($\langle \tau_{11}\rangle > \langle \tau_{33}\rangle$). The anisotropy of $\langle \tau_{ij}|\boldsymbol{u}^r\rangle$ is further discussed in § 3.3. Further understanding of the trends for the conditional SGS normal stress can be gained from the results for the SGS stress production discussed in the following.

The results for the normal components of the conditional production rate $\langle P_{\alpha\alpha}|\boldsymbol{u}^r\rangle$ (no summation), which contains the energy transfer terms, are shown in figure 5(*a–c*).

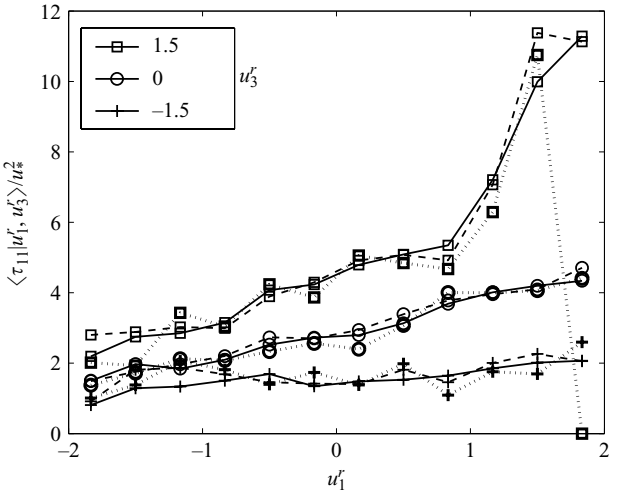

FIGURE 3. Convergence of the conditional SGS stress component $\langle \tau_{11}|u_1^r, u_3^r\rangle$. The dotted, dashed and solid lines represent the results obtained using one-fifth, one-half and the full data set, respectively.

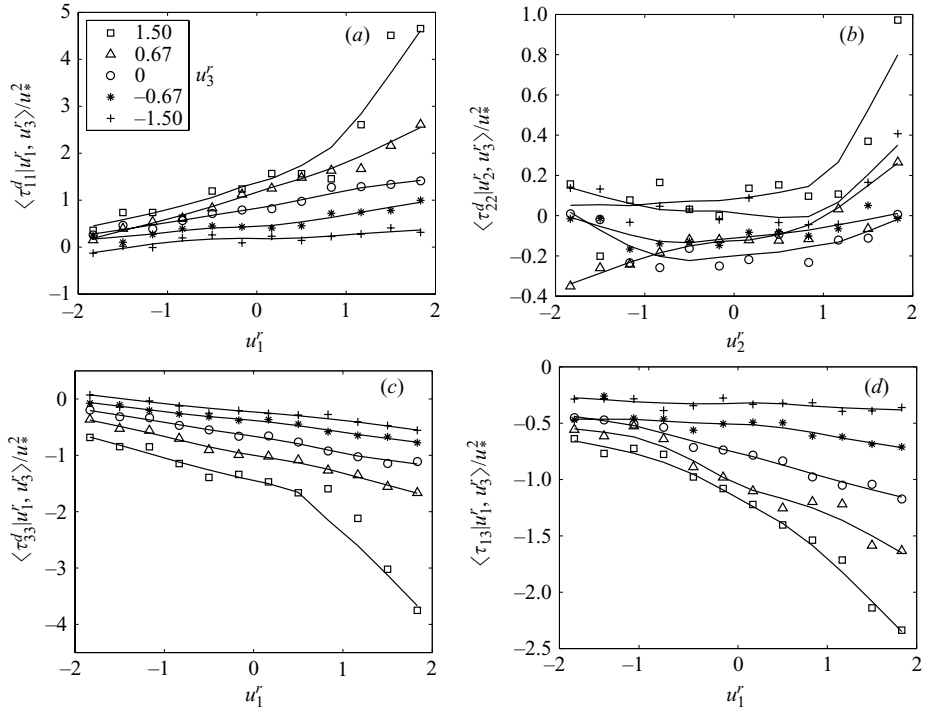

FIGURE 4. Conditional means of the measured deviatoric SGS stress components conditional on the resolvable-scale velocity components. The normal component $\langle \tau_{33}^d|u_1^r, u_3^r\rangle$ generally has the opposite sign as $\langle \tau_{33}|u_1^r, u_3^r\rangle$ owing to the strong anisotropy of the SGS stress.

Similar to $\langle \tau_{11}|u_1^r, u_3^r\rangle$, $\langle P_{11}|u_1^r, u_3^r\rangle$ also increases with u_3^r. It also increases with u_1^r and the dependence on u_1^r is enhanced by positive u_3^r and weakened by negative u_3^r. Figure 5(*c*) shows that $\langle P_{33}|u_1^r, u_3^r\rangle$ decreases with u_3^r and its dependence on u_1^r

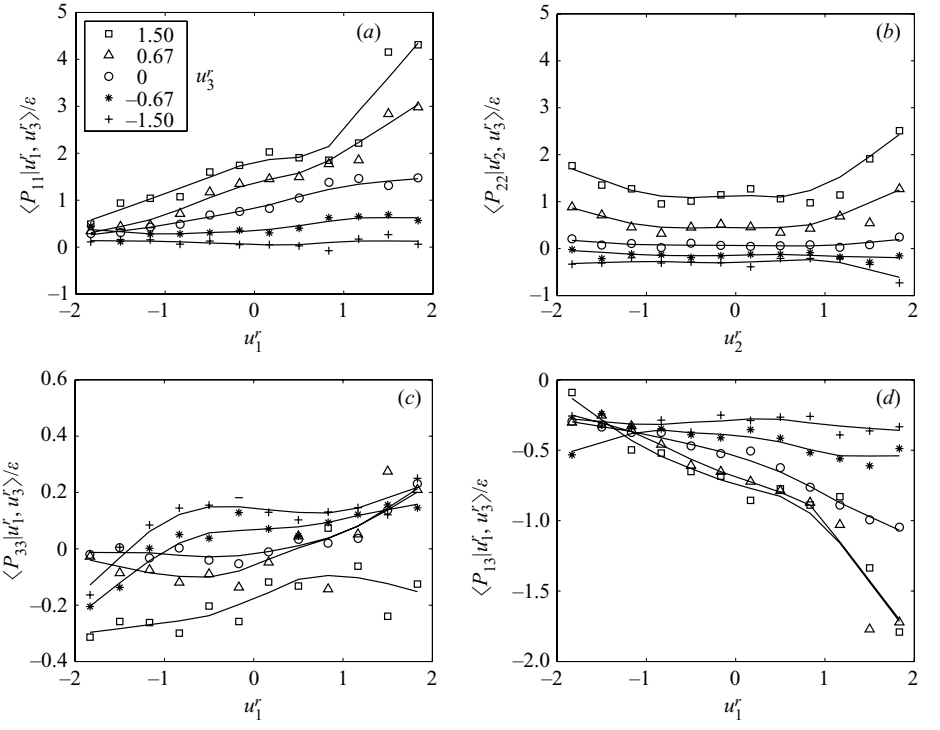

FIGURE 5. Conditional means of the measured SGS stress production components conditional on the resolvable-scale velocity components.

is generally weak, especially for negative u_3^r. Similar to $\langle \tau_{22}|u_2^r, u_3^r\rangle$, $\langle P_{22}|u_2^r, u_3^r\rangle$ also increases with $|u_2^r|$. These trends can be understood in terms of the dynamics of the unstable surface layer and are discussed below.

We first examine the decomposition of $\langle P_{ij}|\boldsymbol{u}^r\rangle$ into $\langle P_{ij}^d|\boldsymbol{u}^r\rangle$ and $\langle -\frac{2}{3}\tau_{kk}S_{ij}|\boldsymbol{u}^r\rangle$. Figure 6(*a*) shows that the trend and magnitude of $\langle P_{11}^d|u_1^r, u_3^r\rangle$ are similar to those of $\langle P_{11}|u_1^r, u_3^r\rangle$ (figure 5*a*), indicating that the conditional spectral transfer part of $\langle P_{11}|\boldsymbol{u}^r\rangle$ dominates over the redistribution part. Figure 6(*b*) shows that $\langle P_{33}^d|u_1^r, u_3^r\rangle$ weakly depends on u_1^r and increases with u_3^r. For negative u_3^r ($u_3^r < -0.5$), $\langle P_{33}^d|u_1^r, u_3^r\rangle$ is negative, indicating conditional backscatter. Notice that the dependence of $\langle P_{33}^d|u_1^r, u_3^r\rangle$ has the opposite trend to that of $\langle P_{33}|u_1^r, u_3^r\rangle$ owing to the redistribution term $\langle -\frac{2}{3}\tau_{kk}S_{33}|u_1^r, u_3^r\rangle$ (see below). The conditional energy transfer rate (figure 6*e*) shows a similar trend to $\langle P_{11}^d|u_1^r, u_3^r\rangle$ and is forward for $u_3^r > 0$. It decreases monotonically as u_3^r moves toward negative values. It is likely that for large negative u_3^r values, the conditional energy transfer will reverse direction (conditional backscatter). These observations are somewhat similar to those of Piomelli, Yu & Adrian (1996) in DNS of a plane channel flow that forward transfer and backscatter are associated with ejections and sweeps, respectively. Sullivan *et al.* (2003) showed that the average amount of backscatter increased with the ratio of the vertical-velocity integral length scale to the filter scale. The results shown here are for the most anisotropic filter in the present study, i.e. for the smallest length-scale ratio; therefore, for the data collected using the other array configurations under similar stability conditions, we expect larger amounts of conditional backscatter. Because conditional backscatter has qualitatively different effects on the evolution of the JPDF than conditional forward

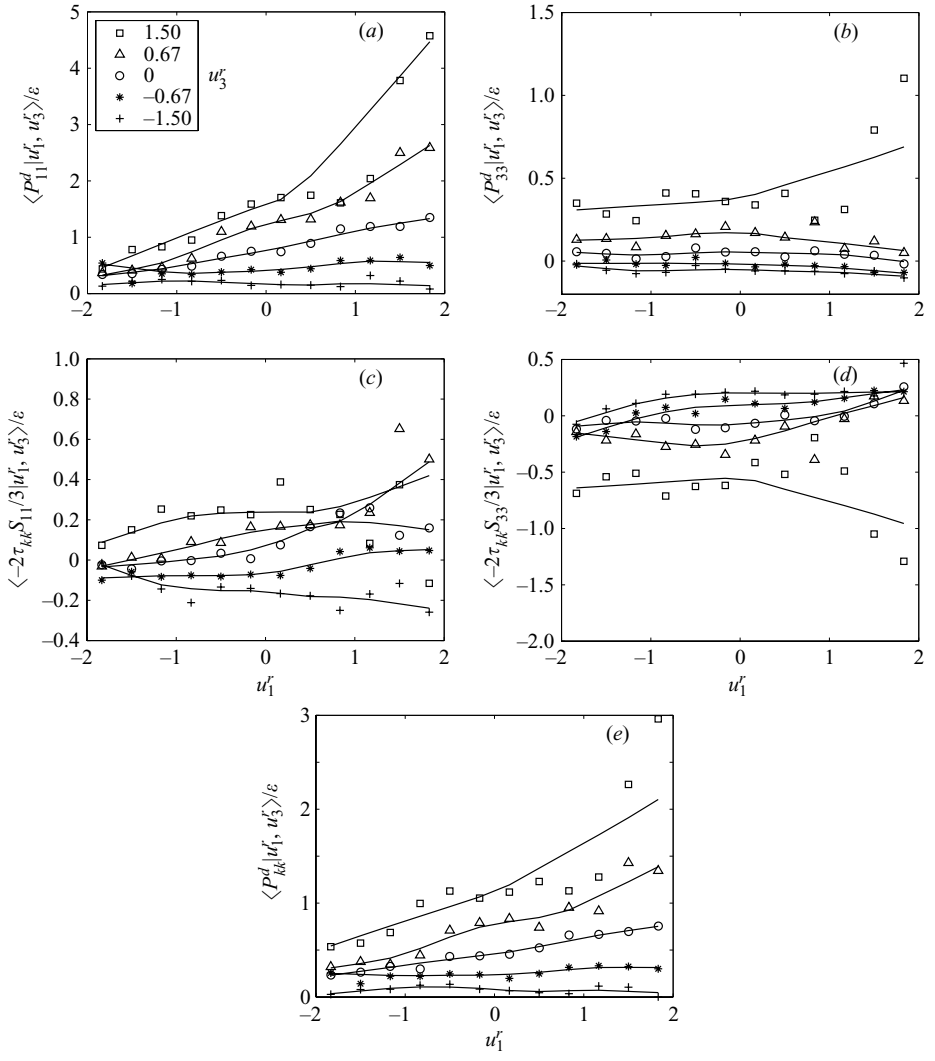

FIGURE 6. Conditional means of the measured production rates of the normal SGS stress components due to: (a, b) the deviatoric part of the SGS stress (τ_{ij}^d); (c, d) the isotropic part ($\tau_{kk}s_{ij}/3$, the redistribution term); (e) the conditional energy transfer rate. Conditional backscatter is evident in (b).

transfer, it is important for SGS models to predict conditional backscatter. Therefore, stochastic backscatter models will not be sufficient if they do not predict correctly the conditional backscatter.

The redistribution terms $\langle -\frac{2}{3}\tau_{kk}S_{11}|u_1^r, u_3^r\rangle$ and $\langle -\frac{2}{3}\tau_{kk}S_{33}|u_1^r, u_3^r\rangle$ are shown in figures 6(c) and 6(d), respectively. Figure 6(c) shows that $\langle -\frac{2}{3}\tau_{kk}S_{11}|u_1^r, u_3^r\rangle$ depends weakly on u_1^r, but increases with u_3^r. It has the same sign as u_3^r, indicating that τ_{11} loses energy to τ_{33} for negative u_3^r and gains energy for positive u_3^r owing to redistribution. Figure 6(d) shows that $\langle -\frac{2}{3}\tau_{kk}S_{33}|u_1^r, u_3^r\rangle$ has a similar trend and magnitude to $\langle -\frac{2}{3}\tau_{kk}S_{11}|u_1^r, u_3^r\rangle$, but has the opposite sign to u_3^r, indicating that τ_{33} gains energy for negative u_3^r and loses energy for positive u_3^r.

To further understand the conditional SGS stress production rate and its relationship to the surface-layer dynamics, we expand $\langle P_{11}|\boldsymbol{u}^r\rangle$ and $\langle P_{33}|\boldsymbol{u}^r\rangle$ into individual SGS stress and velocity gradient terms and examine their relative contributions. Such analyses are useful for identifying the surface-layer processes that contribute to these statistics to guide SGS modelling. From (1.5), $\langle P_{11}|\boldsymbol{u}^r\rangle$ can be expanded as:

$$\langle P_{11}|\boldsymbol{u}^r\rangle = -2\left\langle \tau_{11}^d \frac{\partial u_1^r}{\partial x_1} + \tfrac{1}{3}\tau_{kk}\frac{\partial u_1^r}{\partial x_1} + \tau_{12}\frac{\partial u_1^r}{\partial x_2} + \tau_{13}\frac{\partial u_1^r}{\partial x_3}\middle|\boldsymbol{u}^r\right\rangle. \tag{3.1}$$

The first term on the right-hand side of (3.1) is the conditional energy transfer from resolvable to subgrid-scales associated with the normal strain rate and the normal SGS stress. The second is the conditional inter-component exchange (redistribution). The last two terms are the conditional energy transfer associated with the SGS shear stress and strain components. Our results obtained from the data show that all the terms on the right-hand-side of (3.1) are of the same order of magnitude; therefore, we will discuss the results for each of them. Similarly, $\langle P_{33}|\boldsymbol{u}^r\rangle$ can be expanded as:

$$\langle P_{33}|\boldsymbol{u}^r\rangle = -2\left\langle \tau_{33}^d \frac{\partial u_3^r}{\partial x_3} + \tfrac{1}{3}\tau_{kk}\frac{\partial u_3^r}{\partial x_3} + \tau_{31}\frac{\partial u_3^r}{\partial x_1} + \tau_{32}\frac{\partial u_3^r}{\partial x_2}\middle|\boldsymbol{u}^r\right\rangle. \tag{3.2}$$

The terms on the right-hand side of (3.2) are similar to those in (3.1). However, the results (not shown) indicate that the spectral transfer associated with the shear stress is much smaller than that associated with the normal stress and the inter-component exchange. This is because the derivatives of u_3^r in the horizontal directions ($\partial u_3^r/\partial x_1$ and $\partial u_3^r/\partial x_2$) are small compared to its vertical derivative. Therefore, we will focus on two parts of $\langle P_{33}|\boldsymbol{u}^r\rangle$, $\langle -2\tau_{33}^d(\partial u_3^r/\partial x_3)|\boldsymbol{u}^r\rangle$ and $\langle -\frac{2}{3}\tau_{kk}(\partial u_3^r/\partial x_3)|\boldsymbol{u}^r\rangle$, which are an energy transfer term and the inter-component exchange term, respectively.

We now discuss the results for the components of $\langle P_{11}|u_1^r, u_3^r\rangle$ and $\langle P_{33}|u_1^r, u_3^r\rangle$. The results for positive and negative u_3^r will be discussed separately because these components have qualitatively different characteristics owing to the different surface-layer dynamics associated with updrafts and downdrafts. When u_3^r is positive, vertical-velocity energy-containing eddies move upward and are, on average, stretched in the vertical direction owing to buoyancy acceleration, i.e. $\partial u_3^r/\partial x_3 > 0$. At the same time, continuity requires the eddies, on average, to be compressed in the horizontal direction, i.e. $\partial u_1^r/\partial x_1 < 0$ and $\partial u_2^r/\partial x_2 < 0$. Therefore, the spectral transfer terms associated with the normal strain, $\langle -2\tau_{33}^d(\partial u_3^r/\partial x_3)|u_1^r, u_3^r\rangle$ and $\langle -2\tau_{11}^d(\partial u_1^r/\partial x_1)|u_1^r, u_3^r\rangle$ (not shown) are positive because $\tau_{33}^d < 0$ and $\tau_{11}^d > 0$ owing to the strong anisotropy in the surface layer ($\langle\tau_{11}\rangle > \langle\tau_{33}\rangle$), indicating that both τ_{11} and τ_{33} gain energy (forward transfer) through the spectral transfer associated with the normal strain rates. The inter-component exchange terms, however, have opposite signs with $\langle -\frac{2}{3}\tau_{kk}(\partial u_3^r/\partial x_3)|u_1^r, u_3^r\rangle$ being negative and $\langle -\frac{2}{3}\tau_{kk}(\partial u_1^r/\partial x_1)|u_1^r, u_3^r\rangle$ being positive, indicating that τ_{33} loses energy to τ_{11} through inter-component exchange. Because $\langle -\frac{2}{3}\tau_{kk}(\partial u_3^r/\partial x_3)|u_1^r, u_3^r\rangle$ has a larger magnitude than $\langle -2\tau_{33}^d(\partial u_3^r/\partial x_3)|u_1^r, u_3^r\rangle$, τ_{33} loses more energy owing to the inter-component exchange than it gains from the spectral transfer, resulting in negative $\langle P_{33}|u_1^r, u_3^r\rangle$ values.

The processes described above are enhanced with increasing u_3^r, making the magnitudes of $\langle -\frac{2}{3}\tau_{kk}(\partial u_1^r/\partial x_1)|u_1^r, u_3^r\rangle$ and $\langle -2\tau_{11}^d(\partial u_1^r/\partial x_1)|u_1^r, u_3^r\rangle$ (components of $\langle P_{11}|u_1^r, u_3^r\rangle$) and $\langle P_{33}|u_1^r, u_3^r\rangle$ larger. This is due to two aspects of the surface-layer dynamics. First, a larger u_3^r generally corresponds to stronger buoyancy acceleration, therefore larger vertical stretching and larger magnitudes of $\partial u_3^r/\partial x_3$ and $\partial u_1^r/\partial x_1$

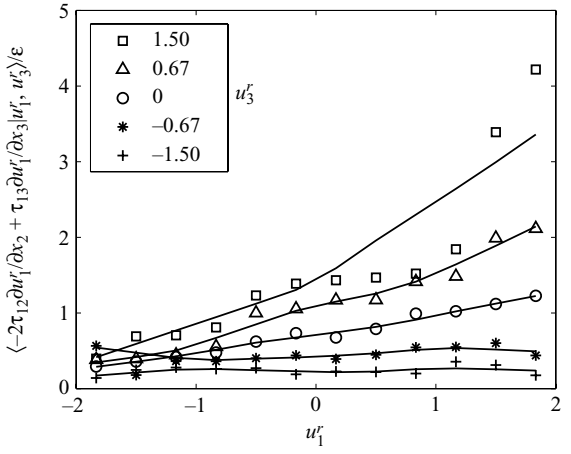

FIGURE 7. Components of $\langle P_{11}|u_1^r, u_3^r\rangle$ due to the shear stress components conditional on the resolvable-scale velocity, which are responsible for the dependence of $\langle P_{11}|u_1^r, u_3^r\rangle$ on u_1^r.

(not shown). Second, the local SGS stress is generally enhanced by positive u_3^r due to eddies with a larger amount of SGS energy brought up from near the ground. This is an advection effect discussed above. Therefore, $\langle -\frac{2}{3}\tau_{kk}(\partial u_1^r/\partial x_1)|u_1^r, u_3^r\rangle$ and $\langle -2\tau_{11}^d(\partial u_1^r/\partial x_1)|u_1^r, u_3^r\rangle$ (components of $\langle P_{11}|u_1^r, u_3^r\rangle$) and the magnitude of $\langle P_{33}|u_1^r, u_3^r\rangle$ generally increase with positive u_3^r.

The spectral transfer terms $\langle -2\tau_{33}^d(\partial u_3^r/\partial x_3)|u_1^r, u_3^r\rangle$ and $\langle -2\tau_{11}^d(\partial u_1^r/\partial x_1)|u_1^r, u_3^r\rangle$ depend only weakly on u_1^r. The inter-component-exchange terms also have similar dependences (not shown). This is because $\partial u_3^r/\partial x_3$ and $\partial u_1^r/\partial x_1$ have weak dependences on u_1^r. Consequently, $\langle P_{33}|u_1^r, u_3^r\rangle$, $\langle -\frac{2}{3}\tau_{kk}(\partial u_1^r/\partial x_1)|u_1^r, u_3^r\rangle$, and $\langle -2\tau_{11}^d(\partial u_1^r/\partial x_1)|u_1^r, u_3^r\rangle$ (components of $\langle P_{11}|u_1^r, u_3^r\rangle$) generally depend weakly on u_1^r. This indicates that the dependence of $\langle P_{11}|u_1^r, u_3^r\rangle$ on u_1^r shown in figure 5(*a*) is due to the shear production components $-2\langle\tau_{12}(\partial u_1^r/\partial x_2) + \tau_{13}(\partial u_1^r/\partial x_3)|u_1^r, u_3^r\rangle$ (figure 7), which have positive contributions to $\langle P_{11}|\boldsymbol{u}^r\rangle$. Both terms depend on u_1^r because when u_3^r is positive, a larger u_1^r on average results in a larger shear strain rate, $\partial u_1^r/\partial x_3$, and at the same time enhances the SGS shear stress component τ_{13}. Thus, $\langle P_{11}|u_1^r, u_3^r\rangle$ is positive and generally depends on u_1^r. Increasing u_3^r on average enhances the SGS shear stress components τ_{13} owing to the advection effect, and enhances $\partial u_1^r/\partial x_3$ owing to the large horizontal velocity deficit carried by fluid brought up from near the ground, making the shear production of the $\langle P_{11}|u_1^r, u_3^r\rangle$ larger. Therefore, $\langle P_{11}|u_1^r, u_3^r\rangle$ generally increases with u_3^r.

The results for negative u_3^r can also be understood in terms of the surface-layer dynamics. When u_3^r is negative, the vertical-velocity energy-containing eddies associated with the returning flow of large convective eddies move downward and are on average compressed in the vertical direction owing to the presence of the ground, resulting in negative $\partial u_3^r/\partial x_3$ and positive $\partial u_1^r/\partial x_1$ and $\partial u_2^r/\partial x_2$. Therefore, the spectral transfer associated with both the normal strain $\langle -2\tau_{33}^d(\partial u_3^r/\partial x_3)|u_1^r, u_3^r\rangle$ and $\langle -2\tau_{11}^d(\partial u_1^r/\partial x_1)|u_1^r, u_3^r\rangle$ are negative, indicating that both τ_{11} and τ_{33} lose energy through spectral transfer associated with the normal strain (conditional backscatter). Similar to the case of $u_3^r > 0$, the inter-component-exchange terms still have opposite signs, but with $\langle -\frac{2}{3}\tau_{kk}(\partial u_3^r/\partial x_3)|u_1^r, u_3^r\rangle$ being positive and $\langle -\frac{2}{3}\tau_{kk}(\partial u_1^r/\partial x_1)|u_1^r, u_3^r\rangle$ being negative, indicating that τ_{33} gains energy from τ_{11} through inter-component exchange. Because $\langle -\frac{2}{3}\tau_{kk}(\partial u_3^r/\partial x_3)|u_1^r, u_3^r\rangle$ has a larger magnitude than

$\langle -2\tau_{33}^d(\partial u_3^r/\partial x_3)|u_1^r, u_3^r\rangle$, τ_{33} gains more energy than it loses due to conditional backscatter, resulting in positive $\langle P_{33}|u_1^r, u_3^r\rangle$ values.

These processes are also somewhat enhanced by larger (negative) u_3^r, although to a much lesser extent than positive u_3^r, resulting in larger magnitudes of $\langle -\frac{2}{3}\tau_{kk}(\partial u_1^r/\partial x_1)|u_1^r, u_3^r\rangle$ and $\langle -2\tau_{11}^d(\partial u_1^r/\partial x_1)|u_1^r, u_3^r\rangle$ (components of $\langle P_{11}|u_1^r, u_3^r\rangle$) and $\langle P_{33}|u_1^r, u_3^r\rangle$. This is because a stronger downdraft (returning flow of large convective eddies) generally produces larger vertical compression, i.e. larger magnitudes of $\partial u_3^r/\partial x_3$ and $\partial u_1^r/\partial x_1$. However, since the eddies carried by returning flow generally have larger length scales, they contain smaller SGS stress (τ_{11}^d, τ_{33}^d and τ_{kk}). Therefore, although the magnitudes of $\langle -\frac{2}{3}\tau_{kk}(\partial u_1^r/\partial x_1)|u_1^r, u_3^r\rangle$ and $\langle -2\tau_{11}^d(\partial u_1^r/\partial x_1)|u_1^r, u_3^r\rangle$ (components of $\langle P_{11}|u_1^r, u_3^r\rangle$) and $\langle P_{33}|u_1^r, u_3^r\rangle$ generally increase with the magnitude of u_3^r, the dependence is not as strong as for the case of positive u_3^r because of these competing effects, and because of the milder vertical compression due to the downdrafts than that due to updrafts (buoyancy acceleration).

When u_3^r is negative, $\langle P_{33}|u_1^r, u_3^r\rangle$, $\langle -\frac{2}{3}\tau_{kk}(\partial u_1^r/\partial x_1)|u_1^r, u_3^r\rangle$ and $\langle -2\tau_{11}^d(\partial u_1^r/\partial x_1)|u_1^r, u_3^r\rangle$ (components of $\langle P_{11}|u_1^r, u_3^r\rangle$) generally depend weakly on u_1^r for reasons similar to those for the case of positive u_3^r. In contrast to the case of positive u_3^r, the shear production components $-2\langle \tau_{12}(\partial u_1^r/\partial x_2) + \tau_{13}(\partial u_1^r/\partial x_3)|u_1^r, u_3^r\rangle$ (figure 7) also depend weakly on u_1^r. This is because both the horizontal shear strain rate component, $\partial u_1^r/\partial x_3$, and the SGS shear stress component, τ_{13}, depend weakly on u_1^r as the vertical shear is weakened by the returning flow. Therefore, $\langle P_{11}|u_1^r, u_3^r\rangle$ also depends weakly on u_1^r. The shear production has a positive contribution, which is larger than the backscatter associated with the normal strain rates and the loss due to inter-component exchange, resulting in positive $\langle P_{11}|u_1^r, u_3^r\rangle$. Increasing the magnitude of u_3^r causes the shear stress components τ_{13} and shear strain rate component $\partial u_1^r/\partial x_3$ to decrease owing to the advection effect and the horizontal velocity deficit carried by the returning eddies. Therefore, $\langle P_{11}|u_1^r, u_3^r\rangle$ generally decreases with u_3^r.

The trends for $\langle P_{22}|u_2^r, u_3^r\rangle$ (figure 5*b*) are generally similar to those of $\langle P_{11}|u_1^r, u_3^r\rangle$. However, there are several differences. One is that $\langle P_{22}|u_2^r, u_3^r\rangle$ increases with $|u_2^r|$, because the flow is symmetric in the lateral direction. Another difference is that the magnitude of $\langle P_{22}|u_2^r, u_3^r\rangle$ is smaller than that of $\langle P_{11}|u_1^r, u_3^r\rangle$ and is negative when u_3^r has large negative values ($u_3^r < -0.6$) because the shear strain rate $\partial u_2^r/\partial x_3$ is smaller than $\partial u_1^r/\partial x_3$, resulting in smaller spectral transfer associated with shear compared to the case for $\langle P_{11}|u_1^r, u_3^r\rangle$. Thus, $\langle P_{22}|u_2^r, u_3^r\rangle$ is smaller than $\langle P_{11}|u_1^r, u_3^r\rangle$ when u_3^r is positive and becomes negative when u_3^r is strongly negative. Therefore, when u_3^r is negative, τ_{22} loses more energy due to the spectral transfer associated with normal strain and inter-component-exchange than it gains due to spectral transfer associated with shear.

With the above discussions on $\langle P_{\alpha\alpha}|\boldsymbol{u}^r\rangle$, the trends for $\langle \tau_{\alpha\alpha}|\boldsymbol{u}^r\rangle$ become clearer. Because the evolution of $\langle \tau_{11}|u_1^r, u_3^r\rangle$ is dominated by $\langle P_{11}|u_1^r, u_3^r\rangle$, $\langle \tau_{11}|u_1^r, u_3^r\rangle$ has similar trends to $\langle P_{11}|u_1^r, u_3^r\rangle$. For the same reason, $\langle \tau_{22}|u_2^r, u_3^r\rangle$ has similar trends to $\langle P_{22}|u_2^r, u_3^r\rangle$. However, the trends for $\langle \tau_{33}|u_1^r, u_3^r\rangle$ are different from those of $\langle P_{33}|u_1^r, u_3^r\rangle$, because buoyancy production dominates the evolution of τ_{33}. Thus, $\langle \tau_{33}|u_1^r, u_3^r\rangle$ has similar trends to the buoyancy production rate $\langle P_{B33}|u_1^r, u_3^r\rangle$, instead of $\langle P_{33}|u_1^r, u_3^r\rangle$ (figure 8). This suggests that buoyancy effects can potentially play an important role in models of the SGS stress.

To summarize this part of the results, when u_3^r is positive, the energy transfer rates due to both normal and shear strain rates are positive (forward). The former depends strongly on u_3^r, but weakly on u_1^r, whereas the latter depends on both. The inter-component exchange is positive for τ_{11} and τ_{22} and is negative for τ_{33}. When

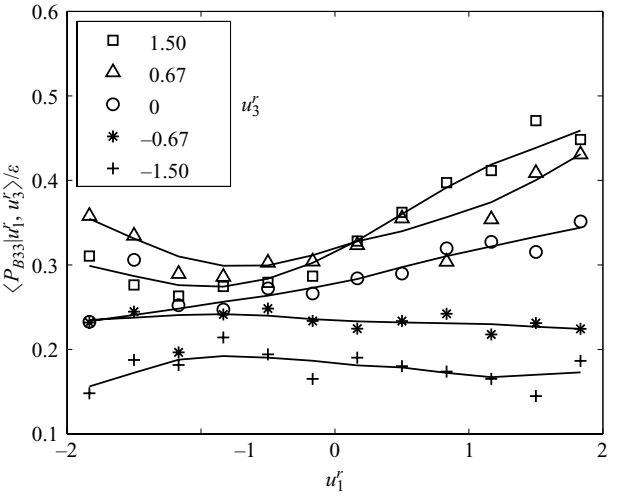

FIGURE 8. The conditional mean of the buoyancy production P_{B33} conditional on the resolvable-scale velocity.

u_3^r is negative, the energy transfer due to the normal strain is negative, whereas that due to shear strain is positive. The dependence on both u_1^r and u_3^r is weaker. The inter-component-exchange terms have opposite signs to those for positive u_3^r. These are closely related to the surface-layer dynamics.

3.2. *Shear components of* $\langle \tau_{ij}|\boldsymbol{u}^r\rangle$ *and* $\langle P_{ij}|\boldsymbol{u}^r\rangle$

The results for the conditional shear stress component $\langle \tau_{13}|u_1^r, u_3^r\rangle$ are shown in figure 4(*d*). The magnitude of $\langle \tau_{13}|u_1^r, u_3^r\rangle$ generally increases with u_3^r. It also increases with u_1^r and the dependence is enhanced by positive u_3^r and weakened by negative u_3^r. To further understand the result of $\langle \tau_{13}|u_1^r, u_3^r\rangle$, we first discuss the result of $\langle P_{13}|u_1^r, u_3^r\rangle$. Figure 5(*d*) shows that the trends of $\langle P_{13}|u_1^r, u_3^r\rangle$ are similar to those of $\langle \tau_{13}|u_1^r, u_3^r\rangle$. The results of $\langle P_{13}|u_1^r, u_3^r\rangle$ can also be understood in terms of the dynamics of the unstable surface layer. We examine the results of $\langle P_{13}^d|u_1^r, u_3^r\rangle$ and $\langle -\frac{2}{3}\tau_{kk}S_{13}|u_1^r, u_3^r\rangle$ which are due to deviatoric and isotropic parts of the SGS stress, respectively (figures 9*a* and 9*b*). Their magnitudes depend on u_1^r and are enhanced by positive u_3^r. The former is positive, indicating destruction of the shear stress, which has negative values, owing to straining and rotation of the anisotropic part of the SGS turbulence. The latter is negative and has about twice the magnitude of the former, indicating production due to straining of the isotropic part of the SGS turbulence.

To understand $\langle P_{13}|\boldsymbol{u}^r\rangle$ in more detail, we expand it as

$$\langle P_{13}|\boldsymbol{u}^r\rangle = -\left\langle \tau_{11}\frac{\partial u_3^r}{\partial x_1} + \tau_{12}\frac{\partial u_3^r}{\partial x_2} + \tau_{13}\frac{\partial u_3^r}{\partial x_3} + \tau_{31}\frac{\partial u_1^r}{\partial x_1} + \tau_{32}\frac{\partial u_1^r}{\partial x_2} + \tau_{33}\frac{\partial u_1^r}{\partial x_3}\middle|\boldsymbol{u}^r\right\rangle. \quad (3.3)$$

Our results obtained from the data show that the first five terms on the right-hand side of (3.3) are small compared to the last term. This is because the derivatives of u_1^r in the horizontal directions and the derivatives of u_3^r are relatively small compared to $\partial u_1^r/\partial x_3$. Therefore, we focus on the last term $\langle -\tau_{33}(\partial u_1^r/\partial x_3)|\boldsymbol{u}^r\rangle$.

The results in § 3.1 have shown that the SGS normal stress τ_{33} and the shear strain rate component $\partial u_1^r/\partial x_3$ increase with u_3^r. They also increase with u_1^r, but the dependence is enhanced by positive u_3^r and weakened by negative u_3^r. Therefore, the magnitude of $\langle P_{13}|\boldsymbol{u}^r\rangle$ also has similar trends. To further understand the trends of

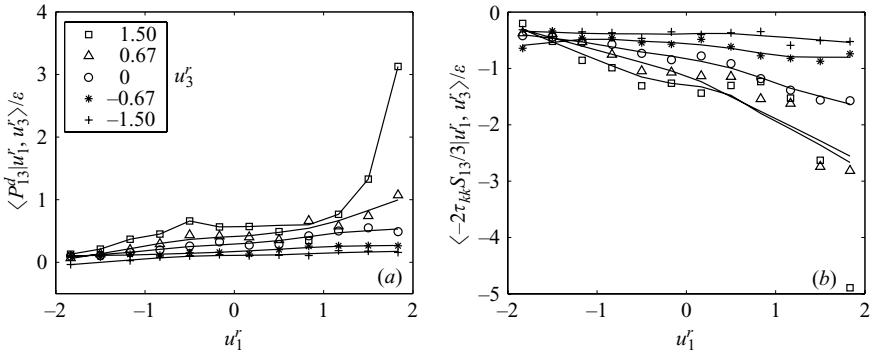

FIGURE 9. Conditional mean of the measured production rate of the shear SGS stress component τ_{13} due to: (*a*) the deviatoric part of the SGS stress (τ_{ij}^d); (*b*) the isotropic part ($\tau_{kk}s_{ij}/3$, the redistribution term). The deviatoric part is generally positive, therefore reduces the SGS shear stress.

$\langle P_{13}|\boldsymbol{u}^r\rangle$, we rewrite $\langle -\tau_{33}(\partial u_1^r/\partial x_3)|\boldsymbol{u}^r\rangle$ as:

$$\left\langle -\tau_{33}\frac{\partial u_1^r}{\partial x_3}\middle|\boldsymbol{u}^r\right\rangle = \left\langle -\tfrac{1}{2}\tau_{33}^d S_{13}\middle|\boldsymbol{u}^r\right\rangle + \left\langle -\tfrac{1}{2}\tau_{33}^d \Omega_{13}\middle|\boldsymbol{u}^r\right\rangle + \left\langle \tfrac{1}{3}\tau_{kk}\frac{\partial u_1^r}{\partial x_3}\middle|\boldsymbol{u}^r\right\rangle, \qquad (3.4)$$

where Ω_{ij} is the rotation tensor of resolvable-scale velocity. The first two terms on the right-hnad side of (3.4) are the conditional shear stress production due to straining and rotation of the anisotropic part of the SGS turbulence. The third is the conditional shear stress production due to the straining of the isotropic part of the SGS turbulence. The trends of $\langle -\frac{1}{2}\tau_{33}^d S_{13}|u_1^r, u_3^r\rangle$ and $\langle -\frac{1}{2}\tau_{33}^d \Omega_{13}|u_1^r, u_3^r\rangle$ (not shown) are similar to that of $\langle P_{13}^d|\boldsymbol{u}^r\rangle$. Their magnitudes are nearly equal and are approximately half of that of $\langle P_{13}^d|u_1^r, u_3^r\rangle$, indicating that the destruction of the conditional shear stress due to rotation, and straining of the anisotropic part of the SGS turbulence are almost equal. Therefore, $\langle P_{13}^d|u_1^r, u_3^r\rangle$ comes primarily from the interactions of τ_{33}^d with the shear strain rate, S_{13}, and the rotation sensor component, Ω_{13}. The trend and magnitude of $\langle -\frac{1}{3}\tau_{kk}(\partial u_1^r/\partial x_3)|u_1^r, u_3^r\rangle$ (not shown) are close to that of $\langle -\frac{2}{3}\tau_{kk}S_{13}|u_1^r, u_3^r\rangle$, indicating that the conditional shear stress production due to straining of isotropic turbulence comes mainly from the interaction of τ_{kk} with the shear strain, S_{13}.

Similarly to $\langle P_{13}|u_1^r, u_3^r\rangle$, $\langle P_{23}|u_2^r, u_3^r\rangle$ comes mainly from the interaction between the normal SGS stress τ_{33} and the horizontal shear $\partial u_2^r/\partial x_3$. The results for $\langle P_{23}|u_2^r, u_3^r\rangle$ are shown in figure 10 and are similar to those of $\langle P_{13}|u_1^r, u_3^r\rangle$. The differences are that the magnitude of $\langle P_{23}|u_2^r, u_3^r\rangle$ increases with $|u_2^r|$ because the flow is symmetric in the lateral direction, and that the magnitude of $\langle P_{23}|u_2^r, u_3^r\rangle$ is smaller than that of $\langle P_{13}|u_1^r, u_3^r\rangle$ because the shear due to u_2^r is smaller than that due to u_1^r.

The evolution of $\langle \tau_{13}|u_1^r, u_3^r\rangle$ is dominated by both $\langle P_{13}|u_1^r, u_3^r\rangle$ and conditional buoyancy production $\langle P_{B13}|u_1^r, u_3^r\rangle$ (figure 11). The conditional buoyancy production $\langle P_{B13}|u_1^r, u_3^r\rangle$ has similar trends and magnitudes to $\langle P_{13}|u_1^r, u_3^r\rangle$. Therefore, $\langle \tau_{13}|u_1^r, u_3^r\rangle$ also has similar trends. Similarly, the evolution of $\langle \tau_{23}|u_2^r, u_3^r\rangle$ (figure 12*a*) is dominated by both $\langle P_{23}|u_2^r, u_3^r\rangle$ and buoyancy production $\langle P_{B23}|u_2^r, u_3^r\rangle$ (figure 12*b*), while $\langle P_{B23}|u_2^r, u_3^r\rangle$ has similar trends and magnitudes to $\langle P_{23}|u_2^r, u_3^r\rangle$. Therefore, $\langle \tau_{23}|u_2^r, u_3^r\rangle$ also has similar trends.

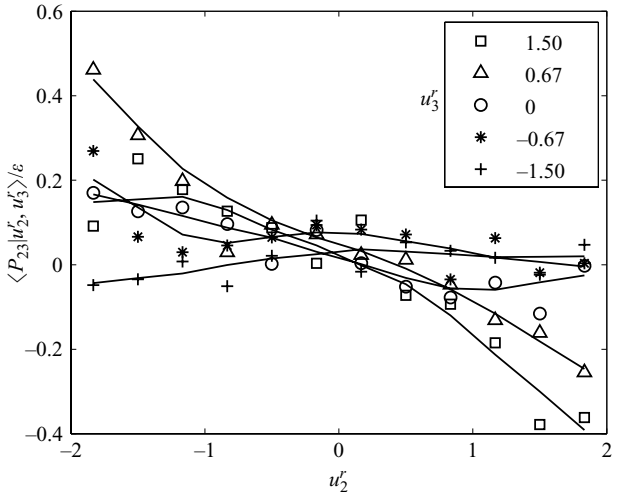

FIGURE 10. Conditional mean of P_{23} conditional on the resolvable-scale velocity components (u_2^r, u_3^r).

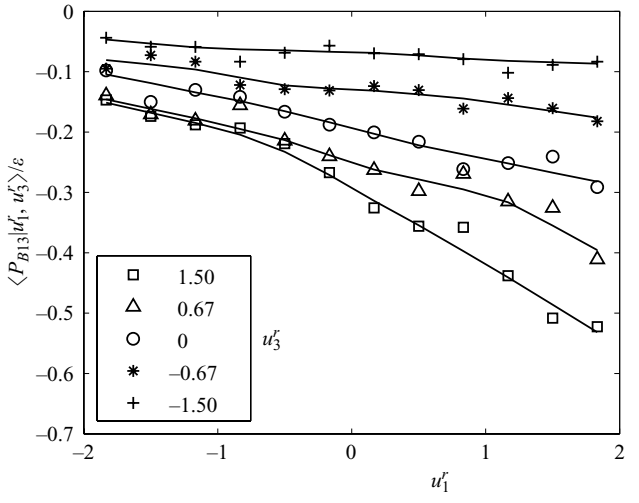

FIGURE 11. Conditional mean of the buoyancy production P_{B13} conditional on the resolvable-scale velocity, which has a similar trend to that of $\langle \tau_{13}|u_1^r, u_3^r\rangle$.

3.3. *Anisotropy of the conditional SGS stress*

An important property of the SGS stress is its level of anisotropy. Sullivan *et al.* (2003) found that the mean SGS stress in the surface layer is generally close to axisymmetric with one large eigenvalue, similar to the Reynolds stress in turbulent boundary layers. It has been argued that the Smagorinsky model under-predicts the anisotropy (redistribution of SGS energy among the normal components) (Kosović 1997).

The level of anisotropy of the conditional SGS stress can be characterized by the representation in the Lumley triangle (Lumley 1978). The normalized anisotropy tensor for $\langle \tau_{ij}|\boldsymbol{u}^r\rangle$,

$$\langle \tau_{ij}^d|\boldsymbol{u}^r\rangle/\langle \tau_{kk}|\boldsymbol{u}^r\rangle = \langle \tau_{ij}|\boldsymbol{u}^r\rangle/\langle \tau_{kk}|\boldsymbol{u}^r\rangle - \tfrac{1}{3}\delta_{ij}, \tag{3.5}$$

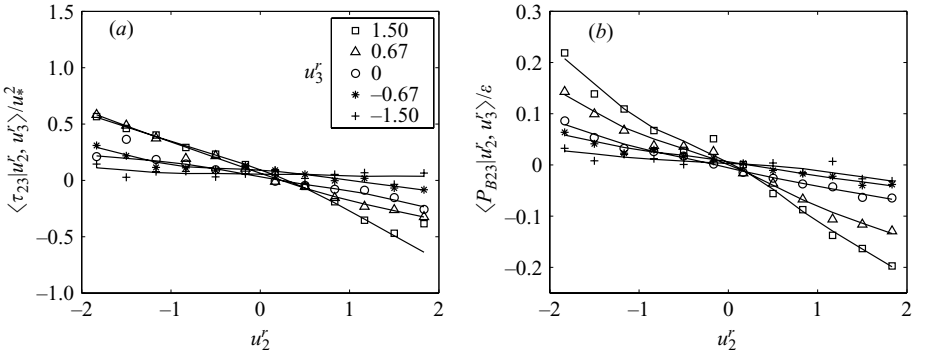

FIGURE 12. Conditional means of (*a*) the measured SGS stress τ_{23}, and (*b*) the conditional buoyancy production P_{B23}, which has a similar trend to that of $\langle \tau_{23}|u_2^r, u_3^r\rangle$.

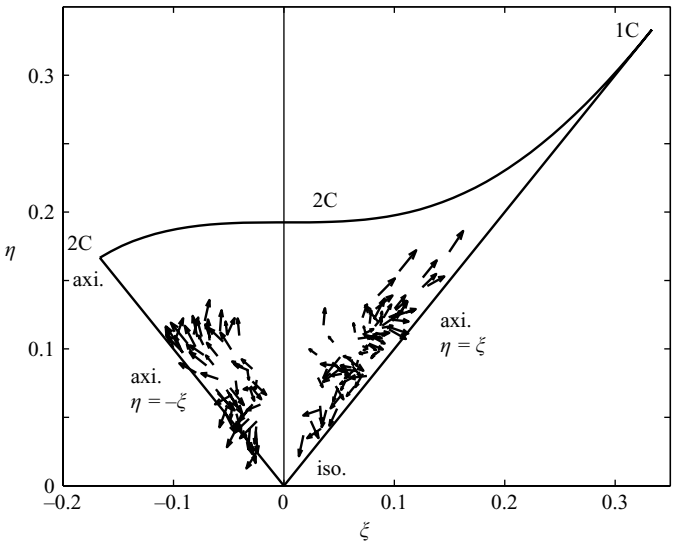

FIGURE 13. Representation of the anisotropy tensor in the Lumley triangle for the conditional SGS stress $\langle \tau_{ij}|u_1^r, u_3^r\rangle$ for array 1 ($\Delta/z = 3.88, -z/L = 0.24$). The arrows represent the conditioning vector (u_1^r, u_3^r). The anisotropy is stronger for $u_3^r > 0$. The SGS stress is close to axiysymmetric with one large and small eigenvalue for $u_1^r > 0$ and $u_1^r < 0$, respectively. 1 C, one-component; 2 C, two-component.

can be determined by two variables ξ and η defined in terms of its invariants (Pope 2000)

$$6\eta^2 = -2II = \langle \tau_{ij}^d|\boldsymbol{u}^r\rangle\langle \tau_{ij}^d|\boldsymbol{u}^r\rangle/\langle \tau_{kk}|\boldsymbol{u}^r\rangle^2, \tag{3.6}$$

$$6\xi^3 = 3III = \langle \tau_{ij}^d|\boldsymbol{u}^r\rangle\langle \tau_{jk}^d|\boldsymbol{u}^r\rangle\langle \tau_{ki}^d|\boldsymbol{u}^r\rangle/\langle \tau_{kk}|\boldsymbol{u}^r\rangle^3, \tag{3.7}$$

where II and III are the second and third invariants of the anisotropy tensor. If $\langle \tau_{ij}|\boldsymbol{u}^r\rangle$ is isotropic, both ξ and η are zero. (The first invariant or trace of $\langle \tau_{ij}^d|\boldsymbol{u}^r\rangle$ is always zero by definition.) The representation for the conditional SGS stress results in figures 2 and 4 is shown in figure 13. There is a clear dependence of the anisotropy on the resolvable-scale velocity. When u_3^r is positive, $\langle \tau_{ij}|u_1^r, u_3^r\rangle$ is quite anisotropic. For negative u_1^r (and positive u_3^r), the points representing the anisotropy are not far from $\eta = -\xi$, indicating that $\langle \tau_{ij}|u_1^r, u_3^r\rangle$ is close to axisymmetric with one small eigenvalue.

Such an SGS stress structure is probably a result of the strong buoyancy effects causing τ_{33} to lose energy to the horizontal components τ_{11} and τ_{22}. As u_1^r increases, the points move toward $\eta = \xi$, indicating that $\langle \tau_{ij} | u_1^r, u_3^r \rangle$ is close to axisymmetric with one large eigenvalue. In addition, as u_1^r and u_3^r both increase, the points appear to move toward the upper right-hand corner, indicating that the conditional SGS stress is approaching the one-component limit. This is probably caused by the strong vertical shear generating elongated structures under such conditions. For negative u_3^r, the points are closer to the origin, indicating that $\langle \tau_{ij} | u_1^r, u_3^r \rangle$ is much less anisotropic. The dependence on u_1^r is also weak, consistent with the results on the conditional SGS stress in figure 4. These results show that not only is there significant anisotropy in $\langle \tau_{ij} | u_1^r, u_3^r \rangle$, but also there are significant variations in the level of anisotropy, which depends on the resolvable-scale velocity. The implications of the anisotropy on LES are discussed in § 5.

We note that the measured invariants, ξ and η, contain statistical uncertainties due to the uncertainties in the measured conditional SGS stress. While the results for $(\xi, \eta) = F(u_1^r, u_3^r)$ are well behaved (surfaces with bumps due to uncertainties), data points with large but similar (u_1^r, u_3^r) can appear at quite different places in the invariant map. This is a manifestation of the uncertainties because the inverse relationship of $(\xi, \eta) = F(u_1^r, u_3^r)$ is shown in the map, suggesting that the results of the invariants for large u_1^r and u_3^r fluctuations are sensitive to the uncertainties in the conditional SGS stress. The sensitivity appears to be higher when u_3^r is negative, at which the magnitude of the conditional SGS stress is small (larger relative uncertainties). Nonetheless, the general trends of the dependence of the anisotropy on the velocity fluctuations are clear on the map.

The results discussed above are for $\Delta/z = 3.88$ and $-z/L = 0.24$ (array 1). Sullivan *et al.* (2003) show that the non-dimensional SGS stress results collapse when plotted as a function of the ratio of the vertical-velocity length scale to the filter size. To examine the effects of Δ/z and $-z/L$ we also obtain the results for the other array configurations. The results for $\langle \tau_{ij} | u_1^r, u_3^r \rangle$ are qualitatively similar to those for array 1, with the dependence on u_3^r generally stronger and the dependence on u_1^r generally weaker. The levels of the anisotropy of $\langle \tau_{ij} | u_1^r, u_3^r \rangle$ for different array configurations are shown in figure 14. When $-z/L$ is fixed, reducing Δ/z (from 2.00 for array 2 to 0.48 for array 4) has essentially no effects on shear and buoyancy. However, an anisotropic grid inherently trends to result in anisotropic SGS stress through anisotropic filtering. Therefore, there is a slight decease in anisotropy in $\langle \tau_{ij} | u_1^r, u_3^r \rangle$ associated with the filter anisotropy. Furthermore, near the surface, anisotropic SGS eddies are affected more strongly by the presence of surface, i.e. the vertical compression due to the returning flows ($u_3^r < 0$) associated with the large convective eddies. The compression effects for array 4 are weaker than those for array 2, resulting in fewer points for the axisymmetric SGS stress with one small eigenvalue ($\eta = -\xi$). A comparison of the levels of anisotropy for array 2 ($\Delta/z = 2.00$, $-z/L = 0.36$) and array 3 ($\Delta/z = 1.00$, $-z/L = 0.60$) shows that $\langle \tau_{ij} | u_1^r, u_3^r \rangle$ for array 3 is less anisotropic than that for array 2, and has very few points near the line of axisymmetric SGS stress with one small eigenvalue ($\eta = -\xi$). The height of array 3 is larger than that of the array 2 (table 1), corresponding to a larger $-z/L$ and a smaller Δ/z. With a larger $-z/L$, the effects of buoyancy are enhanced, but the effects of shear are weakened. These competing effects result in more points for axisymmetric SGS stress with one large eigenvalue ($\eta = \xi$). A smaller Δ/z for array 3 slightly reduces the level of anisotropy in $\langle \tau_{ij} | \boldsymbol{u}^r \rangle$ and the compression effects ($u_3^r < 0$), resulting in fewer points for axisymmetric SGS stress with one small eigenvalue ($\eta = -\xi$). Among the four

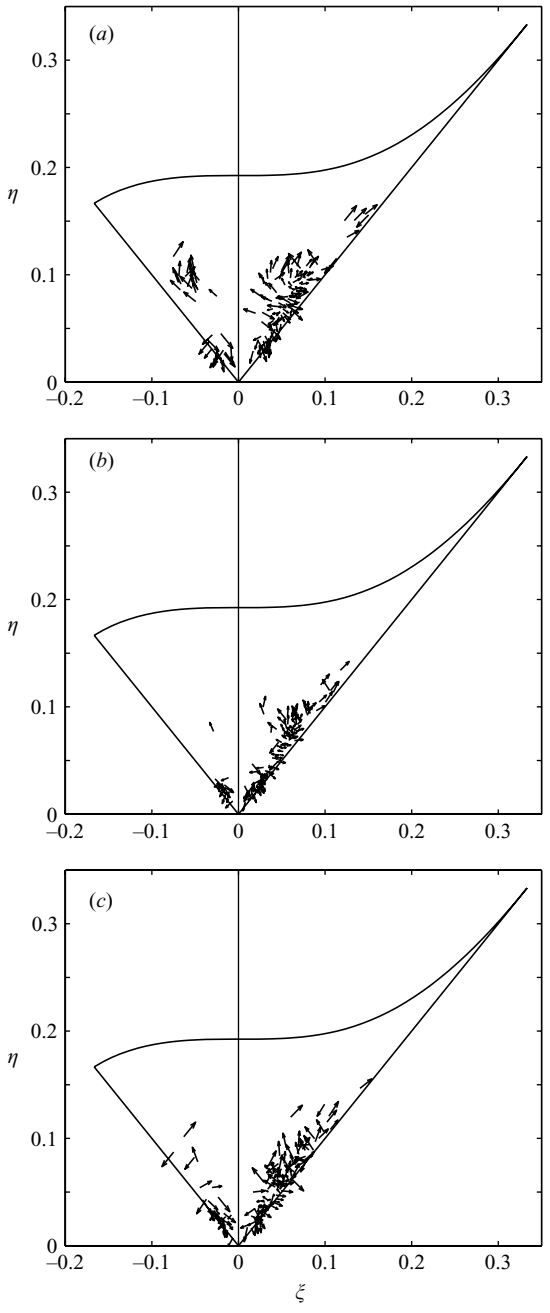

FIGURE 14. The Lumley triangle representation of the conditional SGS stress from other array configurations: (*a*) array 2 ($\Delta/z = 2.00, -z/L = 0.36$); (*b*) array 3 ($\Delta/z = 1.00, -z/L = 0.60$); (*c*) array 4 ($\Delta/z = 0.48, -z/L = 0.35$). The arrows represent the conditioning vector (u_1^r, u_3^r).

arrays, array 1 has the largest Δ/z and the smallest $-z/L$, and consequently has the highest level of anisotropy and the strongest compression effects associated with the returning flow of large convective eddies. Therefore, we expect that the SGS stress and its production rate for array 1 are the most challenging to predict by SGS models.

	$\langle\tau_{11}^d\rangle/u_*^2$	$\langle\tau_{12}\rangle/u_*^2$	$\langle\tau_{13}\rangle/u_*^2$	$\langle\tau_{22}^d\rangle/u_*^2$	$\langle\tau_{23}\rangle/u_*^2$	$\langle\tau_{33}^d\rangle/u_*^2$
τ_{ij}^d	0.79	−0.02	−0.73	−0.04	−0.06	−0.74
τ_{ij}^{smg}	0.02	−0.01	−0.34	0.02	0.01	−0.02
τ_{ij}^{n1}	1.15	−0.04	−0.13	−0.05	0.03	−1.10
τ_{ij}^{mix}	1.16	−0.04	−0.34	−0.03	0.04	−1.12
τ_{ij}^{n2}	0.39	−0.01	−0.33	0.17	0.01	−0.54

TABLE 5. Measured and modelled deviatoric SGS stress for array 1.

Anisotropic grids (refined in the vertical direction), which are often used near the surface to match the flow interior with the surface (e.g. Mason 1994), are therefore of importance. In the following section, we test SGS stress models using data obtained using array 1.

4. SGS stress model predictions

The necessary conditions for predicting the JPDF can be used to test SGS models. In this section, we compute the model predictions of $\langle\tau_{ij}|\boldsymbol{u}^r\rangle$ and $\langle P_{ij}|\boldsymbol{u}^r\rangle$ and compare them to the experimental results for array 1 ($\Delta/z = 3.88$, $-z/L = 0.24$) presented in § 3. We consider the Smagorinsky model, the nonlinear model of Leonard (1974), the mixed model (Vreman, Geurts & Kuerten 1997), and the nonlinear model of Kosović (1997). The average values of the measured and modelled mean deviatoric SGS stress components are given in table 5.

4.1. *Smagorinsky model*

The Smagorinsky model is given by Smagorinsky (1963) and Lilly (1967).

$$\tau_{ij}^{smg} = -2\nu_T S_{ij} = -2(C_s\Delta)^2(2S_{mn}S_{mn})^{1/2}S_{ij}, \tag{4.1}$$

where $C_s = 0.154$ is the Smagorinsky constant for a box filter. In this work, we determine C_s by matching the mean energy transfer rate, i.e. $C_s = \langle P_{ii}^d\rangle/\langle P_{ii}^{smg}\rangle$.

The mean normal SGS stress components are severely under-predicted by the Smagorinsky model and the mean shear stress $\langle\tau_{13}^{smg}\rangle$ is under-predicted by a factor of two. The conditional mean of the model predictions, $\langle\tau_{ij}^{smg}|\boldsymbol{u}^r\rangle$ and $\langle P_{ij}^{smg}|\boldsymbol{u}^r\rangle$ is compared with the conditional mean of the deviatoric part of the SGS stress $\langle\tau_{ij}^d|\boldsymbol{u}^r\rangle$ obtained from the data, because the Smagorinsky model predicts only this part. The predicted normal components of the conditional SGS stress, $\langle\tau_{11}^{smg}|u_1^r, u_3^r\rangle$ (figure 15*a*) and $\langle\tau_{33}^{smg}|u_1^r, u_3^r\rangle$ (figure 15*c*) have weaker trends and smaller magnitudes compared with the measured $\langle\tau_{11}^d|u_1^r, u_3^r\rangle$ (figure 4*a*) $\langle\tau_{33}^d|u_1^r, u_3^r\rangle$ (figure 4*c*). The trends of the production term $\langle P_{11}^{smg}|u_1^r, u_3^r\rangle$ (figures 16*a vs.* 6*a*) are predicted better than those of $\langle\tau_{11}|u_1^r, u_3^r\rangle$. However, the magnitudes are under-predicted (in addition to no conditional backscatter). Since correct prediction of $\langle P_{33}^d|\boldsymbol{u}^r\rangle$ is essential to reproduce the PDF of the vertical resolvable-scale velocity, we plot the results using u_3^r as the independent variable (figure 17*a*). The magnitudes of $\langle P_{33}^d|u_1^r, u_3^r\rangle$ are under-predicted by a factor of two compared with measurements (figure 17*b*), probably because the magnitude of the $\langle\tau_{33}^d|u_3^r\rangle$ is under-predicted by the model. The trend of the SGS shear stress component $\langle\tau_{13}^{smg}|u_1^r, u_3^r\rangle$ (figure 15*d*) compares reasonably well with $\langle\tau_{13}|u_1^r, u_3^r\rangle$ (figure 4*d*). However, the magnitude is under-predicted by a factor of two. The corresponding production rate $\langle P_{13}^{smg}|u_1^r, u_3^r\rangle$ (figures 16*b vs.* 9*a*) is poorly predicted

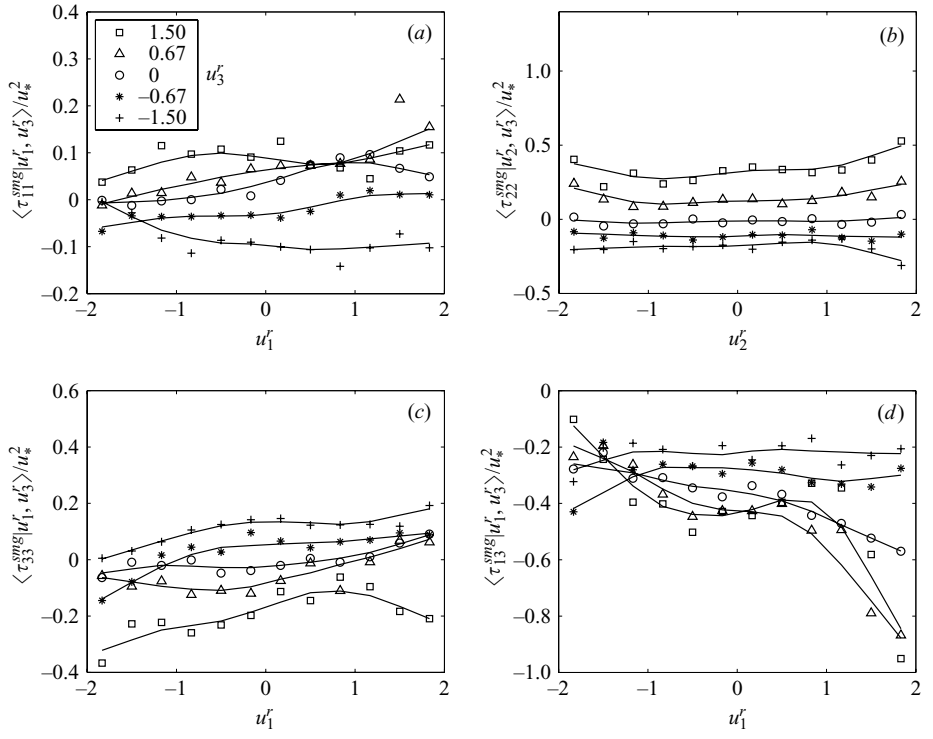

FIGURE 15. Predicted conditional SGS stress using the Smagorinsky model conditional on the resolvable-scale velocity. Only the trend of $\langle \tau_{13} | u_1^r, u_3^r \rangle$ is predicted reasonably well.

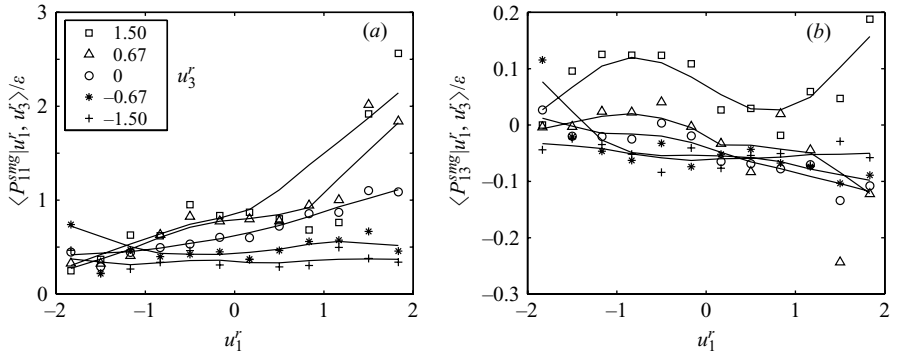

FIGURE 16. Predicted conditional SGS stress production using the Smagorinsky model conditional on the resolvable-scale velocity. Only the trend of $\langle P_{11}^d | u_1^r, u_3^r \rangle$ is predicted reasonably well.

both in terms of magnitude and trend. Therefore, it appears that the standard Smagorinsky model can predict the trends of some SGS shear stress components, but not the normal components, and can predict the trends of some normal components of conditional SGS stress production, but not the shear components. The magnitudes of these components are generally poorly predicted.

The Smagorinsky model predictions can be understood in terms of the surface-layer dynamics and the model ingredients. The results in § 3 show that although

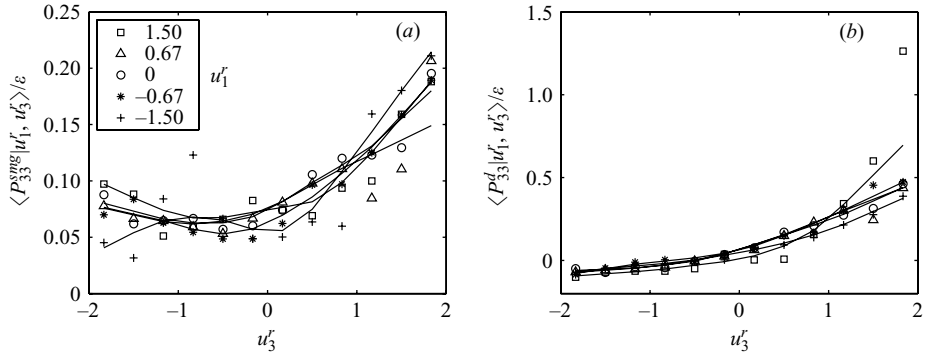

FIGURE 17. Predicted conditional SGS stress production of τ_{33} using the Smagorinsky model conditional on the resolvable-scale velocity.

the evolution (production) of $\langle \tau_{11}^d | u_1^r, u_3^r \rangle$ involves $\partial u_1^r/\partial x_1$, $\partial u_1^r/\partial x_2$ and $\partial u_1^r/\partial x_3$, the shear strain rate component $\partial u_1^r/\partial x_3$ has the most important contribution. However, $\langle \tau_{11}^{smg} | u_1^r, u_3^r \rangle$ is modelled using only $\partial u_1^r/\partial x_1$. Because $\partial u_1^r/\partial x_1$ and $\partial u_1^r/\partial x_3$ have very different behaviours in the surface layer (not shown), neither the magnitude nor trend of $\langle \tau_{11}^{smg} | u_1^r, u_3^r \rangle$ are predicted well. The situation is similar for $\langle \tau_{22}^{smg} | u_2^r, u_3^r \rangle$. The normal component $\langle \tau_{33}^{smg} | u_1^r, u_3^r \rangle$ is also not predicted correctly because the model does not take into account the influence of buoyancy. The predicted trend of $\langle \tau_{13} | u_1^r, u_3^r \rangle$ is somewhat better because the model uses $\partial u_1^r/\partial x_3$, which is also contained in P_{13}; however, because $\langle \tau_{13}^{smg} | \boldsymbol{u}^r \rangle$ does not include the effect of buoyancy, the magnitude is not predicted well.

The Smagorinsky model prediction of the anisotropy tensor is obtained by using the modelled $\langle \tau_{ij}^d | \boldsymbol{u}^r \rangle$ and the measured conditional SGS energy, i.e. it is assumed that the model for the SGS energy used in combination with the Smagorinsky model is accurate. The data points in figure 18(*a*) are much closer to the origin than are the results in figure 13, indicating that the level of anisotropy is severely under-predicted. This is perhaps a reflection of the properties of the resolvable-scale strain rate tensor.

Another variation of the Smagorinsky model uses the SGS kinetic energy to obtain eddy viscosity (Schumann 1975), $\nu_T = C_e \Delta e^{1/2}$ (e is the SGS kinetic energy). This model has been used extensively in large-eddy simulation of the atmospheric boundary layer (Moeng 1984; Shaw & Schumann 1992; Mason 1994). We also computed the predictions of $\langle \tau_{ij}^d | \boldsymbol{u}^r \rangle$ and $\langle P_{ij}^d | \boldsymbol{u}^r \rangle$ using this model. The results are close to those given by (4.1), probably because they both use eddy viscosity and the resolvable-scale strain rate.

4.2. *Nonlinear model*

Bardina, Ferziger & Reynolds (1980) proposed a similarity model, which is based on the scale invariance of inertial-range turbulence. It assumes that the instantaneous SGS stress has similar structures at different scales. The model involves two filters with different filter sizes. Owing to the limitation of the array configuration, we cannot perform this double filtering to test the model. However, the data set allows us to test the nonlinear model, which is the first-order approximation of the similarity model (Leonard 1974; Clark *et al.* 1979).

$$\tau_{ij}^{n1} = \tfrac{1}{12}\Delta^2 \frac{\partial u_i^r}{\partial x_k}\frac{\partial u_j^r}{\partial x_k}, \tag{4.2}$$

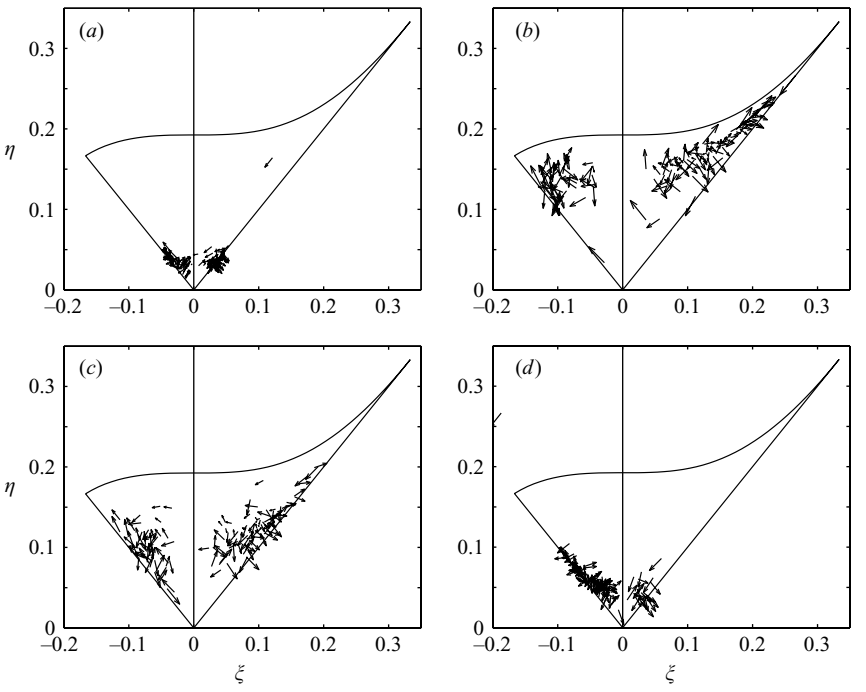

FIGURE 18. The Lumley triangle representation of the conditional SGS stress from SGS models: (*a*) the Smagorinsky model; (*b*) the Nonlinear model; (*c*) the deviatoric mixed model; (*d*) Kosović's nonlinear model. The arrows represent the conditioning vector (u_1^r, u_3^r).

The nonlinear model under-predicts the energy transfer rate by a factor of two and the SGS kinetic energy by 23 % ($\langle \tau_{kk}^{n1} \rangle / u_*^2 = 4.29$ *vs.* $\langle \tau_{kk} \rangle / u_*^2 = 6.27$). The normal mean SGS stress components are generally under-predicted (can be obtained from table 5), but their deviatoric parts are over-predicted (table 5). The conditional SGS stress component $\langle \tau_{11}^{n1} | u_1^r, u_3^r \rangle$ (figure 19*a*) and $\langle \tau_{22}^{n1} | u_2^r, u_3^r \rangle$ (not shown) are only slightly under-predicted whereas $\langle \tau_{33}^{n1} | u_1^r, u_3^r \rangle$ (not shown) are under-predicted by a factor of two. The model also predicts the SGS shear stress $\langle \tau_{13}^{n1} | u_1^r, u_3^r \rangle$ poorly both in terms of the trend and magnitude. On the other hand, the trends for the conditional SGS stress production rate components are predicted quite well ($\langle P_{11}^{n1} | u_1^r, u_3^r \rangle$ is shown in figure 19*b*). Their magnitudes are under-predicted by a factor of two except that of $\langle P_{22}^{n1} | u_2^r, u_3^r \rangle$. Matching the mean energy transfer rate by changing the model coefficient improves the predictions for $\langle P_{ij} | \boldsymbol{u}^r \rangle$, but causes the magnitude of the conditional SGS stress to be over-predicted. Therefore, the nonlinear model also cannot predict the conditional SGS stress and its production rate at the same time.

The nonlinear model predictions can also be understood in terms of the model ingredients and the production of the SGS stress. Because $\langle \tau_{11}^{n1} | \boldsymbol{u}^r \rangle$ involves $\partial u_1^r / \partial x_1$, $\partial u_1^r / \partial x_2$, and $\partial u_1^r / \partial x_3$, which also appear in $\langle P_{11} | u_1^r, u_3^r \rangle$, its trend is better predicted. The situation is similar for $\langle \tau_{22}^{n1} | u_2^r, u_3^r \rangle$. The modelled component $\langle \tau_{33}^{n1} | u_1^r, u_3^r \rangle$ does not include the dominant influence of buoyancy, thus, $\langle \tau_{33} | u_1^r, u_3^r \rangle$ is poorly predicted. Although $\langle \tau_{13}^{n1} | u_1^r, u_3^r \rangle$ involves $\partial u_1^r / \partial x_3$, it is also related to $\partial u_1^r / \partial x_1$ and $\partial u_3^r / \partial x_3$ which are likely to introduce spurious dependence on $\boldsymbol{u}^r$, therefore, $\langle \tau_{13} | u_1^r, u_3^r \rangle$ is also poorly predicted (figure 19*c*).

Unlike the Smagorinsky model, the nonlinear model (figure 18*b*) over-predicts the level of anisotropy. The results are still close to either $\eta = -\xi$ or $\eta = \xi$, i.e.

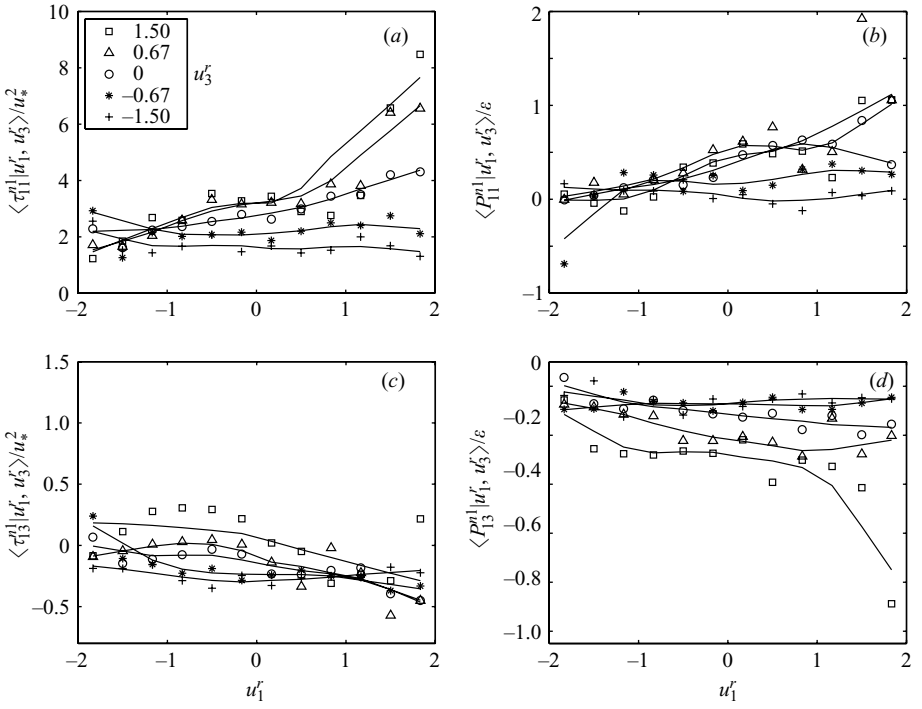

FIGURE 19. Predicted conditional SGS stress and conditional SGS stress production using the nonlinear model conditional on the resolvable-scale velocity. Both $\langle \tau_{11} | u_1^r, u_3^r \rangle$ and $\langle P_{11} | u_1^r, u_3^r \rangle$ are predicted reasonably well.

axisymmetric with one small or large eigenvalue, but are much closer to the two-component axisymmetric or the one-component limits. The lowest predicted level of anisotropy is comparable to the highest measured level. These trends perhaps occur because the nonlinear model contains the resolvable-scale rotation tensor, and therefore contains the effects of the mean rotation.

4.3. *The mixed model*

The above results show that the Smagorinsky model and the nonlinear model under- and over-predict the anisotropy of the conditional SGS stress, respectively. Thus, a mixed model combining these two models (the term 'mixed model' is originally used as the combination of the similarity model and Smagorinsky model):

$$\tau_{ij}^{mix} = \tfrac{1}{12}\Delta^2 \frac{\partial u_i^r}{\partial x_k}\frac{\partial u_j^r}{\partial x_k} - 2(C_s\Delta)^2(2S_{mn}S_{mn})^{1/2}S_{ij} \tag{4.3}$$

can potentially provide improved predictions. The results of Vreman *et al.* (1997) show that this model is better than that of the nonlinear model or Smagorinsky model alone in the large-eddy simulation of a turbulent mixing layer. Here we also test this model. We determine the model coefficients C_s by matching the mean energy transfer rate, i.e. letting $\langle P_{ii} \rangle = \langle P_{ii}^{mix} \rangle$. The results show that the normal components of SGS stress, $\langle \tau_{11} | u_1^r, u_3^r \rangle$ and $\langle \tau_{22} | u_2^r, u_3^r \rangle$, and their production rate, $\langle P_{11} | u_2^r, u_3^r \rangle$ and $\langle P_{22} | u_2^r, u_3^r \rangle$, are generally predicted well. However, the vertical components of $\langle \tau_{ij} | u_1^r, u_3^r \rangle$ and $\langle P_{ij} | u_1^r, u_3^r \rangle$ are under-predicted. For example, comparisons between figures 20(*a*) and 4(*d*) and between figures 20(*b*) and 5(*d*) show that $\langle \tau_{13} | u_1^r, u_3^r \rangle$ and

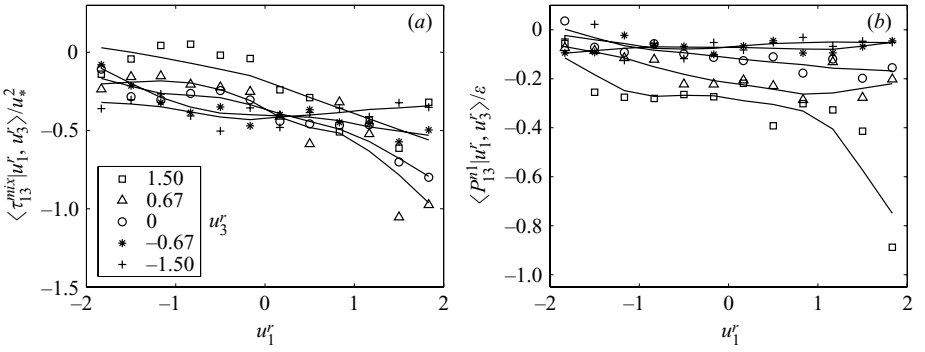

FIGURE 20. Predicted conditional shear SGS stress $\langle \tau_{13} | u_1^r, u_3^r \rangle$ and the conditional production $\langle P_{13} | u_1^r, u_3^r \rangle$ using the mixed model conditional on the resolvable-scale velocity.

$\langle P_{13} | u_1^r, u_3^r \rangle$ are under-predicted. The anisotropy (not shown) is very similar to that of the nonlinear model. Therefore, a linear combination of the nonlinear model and the Smagorinsky model does not significantly improve the predicted conditional means. A problem for this mixed model is that the nonlinear model predicts the total SGS stress, but the Smagorinsky model predicts only the deviatoric part. This suggests that a combination of the deviatoric part of the nonlinear model and the Smagorinsky model might be useful. Therefore, we rewrite the mixed model as:

$$\tau_{ij}^{mix} = \tfrac{1}{12}\Delta^2 \left\{ \frac{\partial u_i^r}{\partial x_k}\frac{\partial u_j^r}{\partial x_k} - \frac{1}{3}\frac{\partial u_m^r}{\partial x_k}\frac{\partial u_m^r}{\partial x_k}\delta_{ij} \right\} - 2(C_s\Delta)^2(2S_{mn}S_{mn})^{1/2}S_{ij}. \tag{4.4}$$

The deviatoric mixed model not only predicts well the normal components of SGS stress, $\langle \tau_{11}^d | u_1^r, u_3^r \rangle$ and $\langle \tau_{22}^d | u_2^r, u_3^r \rangle$, and their production rates, $\langle P_{11}^d | u_1^r, u_3^r \rangle$ and $\langle P_{22}^d | u_2^r, u_3^r \rangle$, but also predicts well $\langle \tau_{33}^d | u_1^r, u_3^r \rangle$ (figure 21*a*) and $\langle P_{33}^d | u_1^r, u_3^r \rangle$ (figure 21*b*), which are under-predicted by the original mixed model. The SGS shear stress production $\langle P_{13}^{mix} | u_1^r, u_3^r \rangle$ (figure 21*c*) is also better predicted than that in figure 20(*b*). Unfortunately, $\langle \tau_{13} | \boldsymbol{u}^r \rangle$ (identical to the mixed model prediction shown in figure 20*a*) remains to be improved, which is a very important component for LES in the surface layer. The predicted anisotropy (figure 18*c*) using the deviatoric mixed model is stronger than measurements, but is improved over that of the nonlinear model. The mixed model over-predicts the (intrinsic) anisotropy, but under-predicts $\langle \tau_{13} | u_1^r, u_3^r \rangle$, suggesting that the directions of the principal axes of $\langle \tau_{ij} | u_1^r, u_3^r \rangle$ are not predicted well. This is in contrast to the Smagorinsky model which under-predicts both. We also experimented by changing the ratio of the two model coefficients (strictly speaking, the coefficient for the nonlinear part is fixed by the filter type) with little effect on the anisotropy.

Another type of cancellation between the Smagorinsky model and the similarity model (Bardina *et al.* 1980) was observed by Liu, Katz & Meneveau (1999) in rapidly strained homogeneous turbulence. There, the under-prediction by the Smagorinsky model and the over-prediction by the similarity model of the mean spectral energy transfer rate during straining were partially cancelled when a mixed model was used. Therefore, it appears that various kinds of opposing trends of the Smagorinsky model and the similarity (and nonlinear) model can be partially cancelled by using a mixed model.

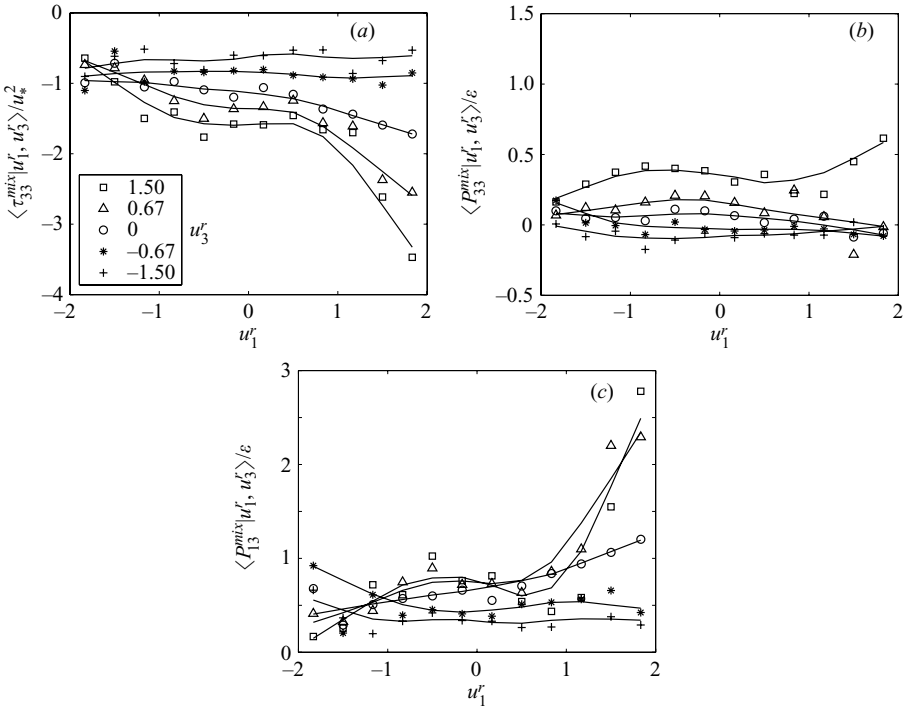

FIGURE 21. Predicted conditional SGS stress and conditional SGS stress production using the deviatoric mixed model conditional on the resolvable-scale velocity. Note that the predicted $\langle \tau_{13} | u_1^r, u_3^r \rangle$ is identical to that of the mixed model.

4.4. *Kosvić's nonlinear model*

Kosović (1997) proposed another nonlinear model:

$$\tau_{ij}^{n2} = -(C_s\Delta)^2 \big\{ 2(2S_{mn}S_{mn})^{1/2} S_{ij} + C_1 \big(S_{ik}S_{kj} - \tfrac{1}{3} S_{mn}S_{mn}\delta_{ij} \big) + C_2 (S_{ik}\Omega_{kj} - \Omega_{ik}S_{kj}) \big\}, \tag{4.5}$$

where C_s, C_1 and C_2 are model constants, which are determined here by matching the mean energy transfer rate, i.e. letting $\langle P_{ii}^d \rangle = \langle P_{ii}^{n2} \rangle$ while maintaining the ratios of their original values in Kosović (1997). The first part of this model is essentially the Smagorinsky model. By setting $C_2 = 0$, this model is essentially the deviatoric mixed model. A comparison between the results of this model (results not shown) and the deviatoric mixed model shows that the latter predicts $\langle \tau_{13} | u_1^r, u_3^r \rangle$ (figure 22) better, but the rest of the components of the conditional SGS stress and the conditional SGS stress production are less well predicted. Therefore, this nonlinear model has a somewhat more balanced overall performance. Like the Smagorinsky model, this nonlinear model under-predicts the magnitude of the conditional SGS stress (by approximately 50 %) when the mean energy transfer is matched. This is probably because this model over-predicts the correlation between the SGS stress and the strain rate. The level of anisotropy of $\langle \tau_{ij} | u_1^r, u_3^r \rangle$ (figure 18*d*) is also under-predicted, but the prediction is improved over that of the Smagorinsky model.

5. Effects of SGS model deficiencies on LES results

The measured conditional SGS stress and the SGS stress production and the model predictions can be used to identify model deficiencies that cause inaccuracies in LES

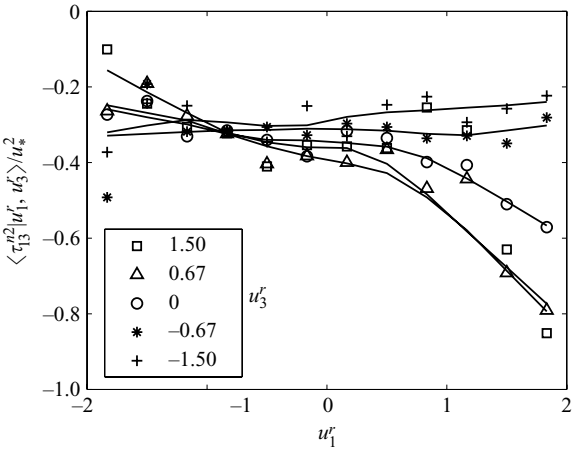

FIGURE 22. Predicted conditional shear SGS stress $\langle \tau_{13} | u_1^r, u_3^r \rangle$ using Kosvić's nonlinear model conditional on the resolvable-scale velocity, which is improved over the mixed model.

results. Previous studies have shown that the Smagorinsky model over-predicts the mean shear and the streamwise velocity variance near the surface (Mason & Thomson 1992; Sullivan *et al.* 1994). We argue that these inaccuracies are at least partly due to the under-prediction of the anisotropy of the SGS stress and its variations in the near-wall region. In the atmospheric boundary layer (ABL), the vertical shear stress component is determined by the geostrophic conditions and the mean shear (Panofsky & Dutton 1984; Wyngaard 1992), which are a combination of the large-scale pressure gradient and the Coriolis force, therefore a simulation tends to adjust itself to satisfy these conditions. Because the anisotropy of the SGS stress (figure 13) is under-predicted, the simulation must generate a larger strain rate to produce the correct SGS shear stress, thereby over-predicting the mean shear. In addition, the larger strain rate will cause over-prediction of the production of the streamwise velocity variance, $-\langle u_1^{r\prime} u_3^{r\prime} \rangle (\partial U_1 / \partial x_3)$, therefore the streamwise velocity variance itself, where $u_i^{r\prime}$ is the fluctuation of u_i^r. Furthermore, the conditional variations of the anisotropy (the SGS shear stress) are also severely under-predicted, further reducing the transfer of the streamwise velocity variance to the subgrid scales.

The stochastic backscatter model of Mason & Thomson (1992) introduces additional energy (on average) into the resolvable scales through random forcing, at the same time increasing the dissipation by eddy viscosity to maintain the energy balance. In doing so, the model is able to predict τ_{13} and anisotropy better without generating an excessive strain rate. In the split model of Sullivan *et al.* (1994), an increasing part of τ_{13} is produced by the mean shear as the surface is approached; therefore the results are less affected by the inability of the Smagorinsky model to predict the anisotropy. The nonlinear model of Kosović (1997) is also capable of producing a higher level of anisotropy (figure 18*d*) and gives improved LES results. Therefore, it appears that the anisotropy of the SGS stress is important for the correct prediction of the mean shear and the streamwise velocity variance.

Another important surface-layer statistic is the vertical velocity skewness, which is under-predicted by LES using the Smagorinsky model (Lemone 1990; Moeng & Rotunno 1990). This can be examined by considering the conditional SGS stress $\langle \tau_{33} | u_3^r \rangle$ and the SGS stress production $\langle P_{33} | u_3^r \rangle$, which appear in the equation for the

resolvable-scale vertical velocity PDF

$$\frac{\partial f_{u_3^r}}{\partial t} + v_3 \frac{\partial f_{u_3^r}}{\partial x_3} = \frac{\partial^2}{\partial v_3 \partial x_3}\left\{\left\langle \tau_{33} \middle| u_3^r = v_3 \right\rangle f_{u_3^r}\right\} + \frac{\partial^2}{\partial v_3 \partial v_3}\left\{-\tfrac{1}{2}\left\langle P_{33} \middle| u_3^r = v_3 \right\rangle f_{u_3^r}\right\} + \frac{\partial^2}{\partial v_3 \partial x_3}\left\{\left\langle p^r \middle| u_3^r = v_3 \right\rangle f_{u_3^r}\right\} + \frac{\partial^2}{\partial v_3 \partial v_3}\left\{\left\langle p^r \frac{\partial u_3^r}{\partial x_3} \middle| u_3^r = v_3 \right\rangle f_{u_3^r}\right\} - \frac{g}{\Theta}\frac{\partial}{\partial v_3}\left\{\left\langle \theta^r \middle| u_3^r = v_3 \right\rangle f_{u_3^r}\right\}, \tag{5.1}$$

where $f_{u_3^r} = \langle \delta(u_3^r - v_3) \rangle$. The mixed transport terms due to the conditional SGS stress and the resolvable-scale pressure are expected to diminish with the filter scale, whereas the terms due to the conditional pressure–strain correlation and the conditional SGS stress production are expected to be invariant for inertial-range filter scales.

The pressure–strain correlation is associated with return to isotropy and partially counters the production. Therefore, the dominant term in the equation is expected to be the conditional SGS stress production. In a quasi-stationary and horizontally homogeneous ABL there is a balance primarily among advection, transport due to conditional pressure–strain correlation, and transport due to the conditional SGS stress production. Sabelnikov (1998) analysed the PDF equation for scalar fluctuations generated by a constant mean scalar gradient and stationary isotropic turbulence and provided a self-similar relationship between the scalar PDF and the conditional scalar dissipation, which plays a similar role to P_{33} in (5.1). He showed that for a conditional dissipation independent of the scalar value, the scalar PDF is Gaussian. If the conditional dissipation increases with the scalar fluctuations, the PDF is super-Gaussian and vice versa. Because of the similarities between (5.1) and the scalar PDF transport equation, these trends are expected to hold qualitatively for (5.1). Therefore, there exists a direct link between the resolvable-scale vertical velocity PDF and $\langle P_{33} | u_3^r \rangle$ for a stationary ABL. Physically, to maintain a longer (or higher) tail of the PDF, the SGS turbulence must extract more energy from the resolvable scales when the velocity fluctuations are large. Figure 17(*b*) shows that the measured $\langle P_{33} | \boldsymbol{u}^r \rangle$ increases with u_3^r, therefore is asymmetric with respect to u_3^r. Consequently, the positive side of $f_{u_3^r}$ is higher than the negative side, resulting in a positive skewness. On the other hand, the prediction of the Smagorinsky model is much less dependent on u_3^r, and consequently will result in a smaller skewness. Therefore, the under-prediction of the vertical velocity skewness is probably due to the inability of the model to predict the asymmetry in $\langle P_{33} | u_3^r \rangle$. The specific model deficiencies identified here can be used to guide development of improved SGS models that will correctly predict these statistics. The analyses in this section and § 3 can serve as examples for studying aspects of SGS turbulence and SGS models that are important for specific applications.

We note that previous *a priori* tests, especially those correlating the modelled to the true SGS stress, have provided little information about how SGS models will perform in a simulation. For example, the Smagorinsky model has very low correlation coefficients with the true SGS stress, but performs quite well in LES of isotropic turbulence whereas the similarity model correlates well with the true stress, but may cause simulations to become unstable. The difficulty in interpreting *a priori* test results and model performance in simulations is partly because there is no equation relating the tests results to LES statistics. In addition, owing to the chaotic nature of the LES equations, a high (unless perfect) correlation between the modelled and true SGS stress cannot guarantee accurate LES statistics. Another

problem of these *a priori* tests is that they focused solely on the SGS stress whereas equation (1.4) shows that the SGS stress production rate is also important. In the case of homogeneous turbulence, the influence of the conditional SGS stress vanishes. In such flows, the conditional mean SGS energy transfer rate (near the mean velocity) plays an dominant role in determining the lower-order LES statistics. Therefore, the Smagorinsky, whose coefficient is determined by matching the inertial-range energy transfer rate to the theoretical values, performs quite well in LES of homogeneous turbulence with a well-resolved energy-containing range despite the low correlation with the true SGS stress. On the other hand, the similarity model under-predicts the (mean and conditional) energy transfer rate, therefore does not perform well (in fact might not be used alone) despite its relatively high correlation with the true SGS stress. In inhomogeneous flows, both the conditional SGS stress and the conditional SGS stress production rate are important. The mixed model makes use of the abilities of the Smagorinsky model to predict the mean energy transfer and of the similarity model to predict the SGS stress, resulting in improved performance. Therefore, *a priori* tests based on the JPDF equation differ fundamentally from the traditional tests and can provide valuable information about model performance.

6. Further analyses of $\langle \tau_{ij} | \boldsymbol{u}^r \rangle$ and $\langle P_{ij} | \boldsymbol{u}^r \rangle$

The results in the present study for the conditional SGS stress $\langle \tau_{ij} | \boldsymbol{u}^r \rangle$ and conditional SGS stress production rate $\langle P_{ij} | \boldsymbol{u}^r \rangle$ show that there are similarities between their trends. The deviatoric parts of $\langle \tau_{ij} | \boldsymbol{u}^r \rangle$ and $\langle P_{ij} | \boldsymbol{u}^r \rangle$ (not shown) also have similar dependence on $\boldsymbol{u}^r$. Wyngaard (1992) showed that the Reynolds shear stress budget in the unstable surface layer is generally in local balance among shear production, buoyancy production, and pressure destruction, whereas turbulent transport is negligible. The (slow) pressure destruction term is usually modelled using Rotta's (1951) 'return-to-isotropy' model,

$$\frac{1}{\rho_0}\left\langle u_i \frac{\partial p}{\partial x_j} + u_j \frac{\partial p}{\partial x_i} \right\rangle \sim \frac{\langle u_i u_j \rangle - \frac{1}{3}\langle u_k u_k \rangle \delta_{ij}}{t_l}, \tag{6.1}$$

where t_l is a time scale, which is of the order of the integral time scale. Therefore, we may expect some similarities between $\langle u_i u_j \rangle - \frac{1}{3}\langle u_k u_k \rangle \delta_{ij}$ and the combination of the shear and buoyancy production. Wyngaard (2004) suggests that the balance between the deviatoric SGS stress and the production can be given as

$$\frac{\tau_{ij}^{mod}}{t_\Delta} = P_{ij}^a, \tag{6.2}$$

where t_Δ is a turbulent time scale and $P_{ij}^a = P_{ij} - \frac{1}{3}P_{kk}\delta_{ij}$ is the anisotropic part of the SGS stress production tensor. Because P_{ij}^a contains τ_{ij}, this relationship could potentially be used as an algebraic SGS model. To investigate this potential, we study the geometric alignment and eigenvalue relationship between $\langle \tau_{ij}^d | \boldsymbol{u}^r \rangle$ and $\langle P_{ij}^a | \boldsymbol{u}^r \rangle$. The effects of advection $u_k^r(\partial \tau_{ij}^d / \partial x_k)$ and buoyancy can also be analysed by adding corresponding terms to the right-hand side of (6.2).

The eigenvalues of the conditional SGS stress tensor, $\langle \tau_{ij}^d | \boldsymbol{u}^r \rangle$, are denoted as α_τ, β_τ and γ_τ, ordered such that $\alpha_\tau \geqslant \beta_\tau \geqslant \gamma_\tau$, and the corresponding unit eigenvectors as $\boldsymbol{\alpha}_\tau$, $\boldsymbol{\beta}_\tau$ and $\boldsymbol{\gamma}_\tau$. Similarly, the eigenvalues of the conditional SGS stress production tensor, $\langle P_{ij}^a | \boldsymbol{u}^r \rangle$, are denoted as α_P, β_P and γ_P, ordered such that $\alpha_P \geqslant \beta_P \geqslant \gamma_P$, and the corresponding unit eigenvectors as $\boldsymbol{\alpha}_P$, $\boldsymbol{\beta}_P$ and $\boldsymbol{\gamma}_P$. In order to characterize

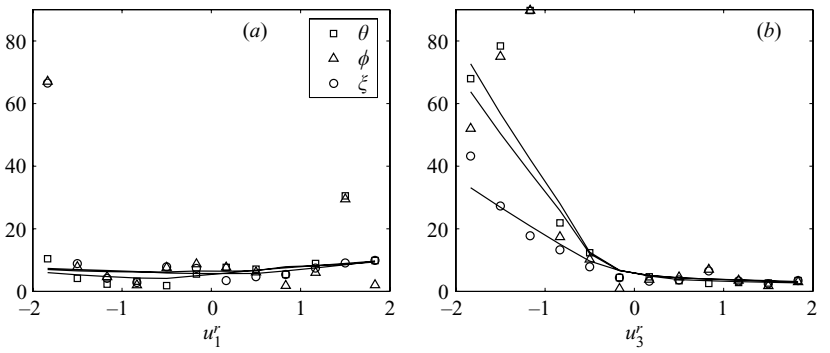

FIGURE 23. Geometric alignment of the measured conditional SGS stress and the conditional SGS stress production conditional on (*a*) u_1^r and (*b*) u_3^r. The alignment angles are small for positive u_3^r and increases for negative u_3^r, but depends weakly on u_1^r.

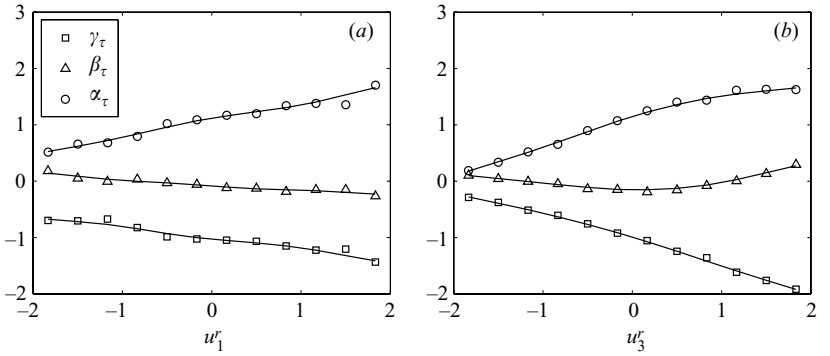

FIGURE 24. Eigenvalues of the conditional SGS stress conditional on (*a*) u_1^r and (*b*) u_3^r. The magnitudes of the eigenvalues increase with the resolvable-scale velocity.

the geometric alignment between the eigenvectors of $\langle \tau_{ij}^d | \boldsymbol{u}^r \rangle$ and $\langle P_{ij}^a | \boldsymbol{u}^r \rangle$, three angles, θ, ϕ and ξ, are defined as $\theta = \cos^{-1}(|\boldsymbol{\gamma}_P \cdot \boldsymbol{\gamma}_\tau|)$ (the angle between $\boldsymbol{\gamma}_P$ and $\boldsymbol{\gamma}_\tau$), $\phi = \cos^{-1}(|\boldsymbol{\beta}_P \cdot \boldsymbol{\beta}_\tau|)$, and $\xi = \cos^{-1}(|\boldsymbol{\alpha}_P \cdot \boldsymbol{\alpha}_\tau|)$.

The geometric alignment results for $\langle \tau_{ij}^d | \boldsymbol{u}^r \rangle$ and $\langle P_{ij}^a | \boldsymbol{u}^r \rangle$ are shown in figure 23. For $\langle \tau_{ij}^d | u_1^r \rangle$ and $\langle P_{ij}^a | u_1^r \rangle$, the values of θ, ϕ and ξ are generally less than 10° and weakly depend on u_1^r, indicating very good alignment. Figure 23(*b*) shows that $\langle \tau_{ij}^d | u_3^r \rangle$ and $\langle P_{ij}^a | u_3^r \rangle$ are aligned well when u_3^r is positive but are less well aligned when u_3^r is negative. Because $\langle \tau_{ij} | \boldsymbol{u}^r \rangle$ is much less anisotropic and $\langle \tau_{ij}^d | u_3^r \rangle$ and $\langle P_{ij}^a | u_3^r \rangle$ are small when u_3^r has large negative values, the alignment angles are less well defined.

We also examine the effects of advection and buoyancy on the conditional SGS stress by including these terms in the alignment calculation. The alignment results for $\langle \tau_{ij}^d | \boldsymbol{u}^r \rangle$ and $\langle P_{ij}^a + A_{ij}^a | \boldsymbol{u}^r \rangle$ and $\langle P_{ij}^a + P_{Bij}^a | \boldsymbol{u}^r \rangle$ are also computed, where A_{ij}^a is the advection term of τ_{ij}^d and $P_{Bij}^a = P_{Bij} - \frac{1}{3} P_{Bkk} \delta_{ij}$. The trends and the magnitudes of the alignment angles (not shown) are very close to those shown figure 23. Therefore, introducing the advection term and the buoyancy production generally has a negligible effect on the geometric alignment.

The eigenvalues of $\langle \tau_{ij}^d | u_1^r \rangle$ and $\langle \tau_{ij}^d | u_3^r \rangle$ conditional on u_1^r and u_3^r are shown in figure 24. The eigenvalues α_τ and γ_τ generally depend on u_1^r and u_3^r, and the magnitudes generally increase with u_1^r and u_3^r, indicating that the SGS turbulence

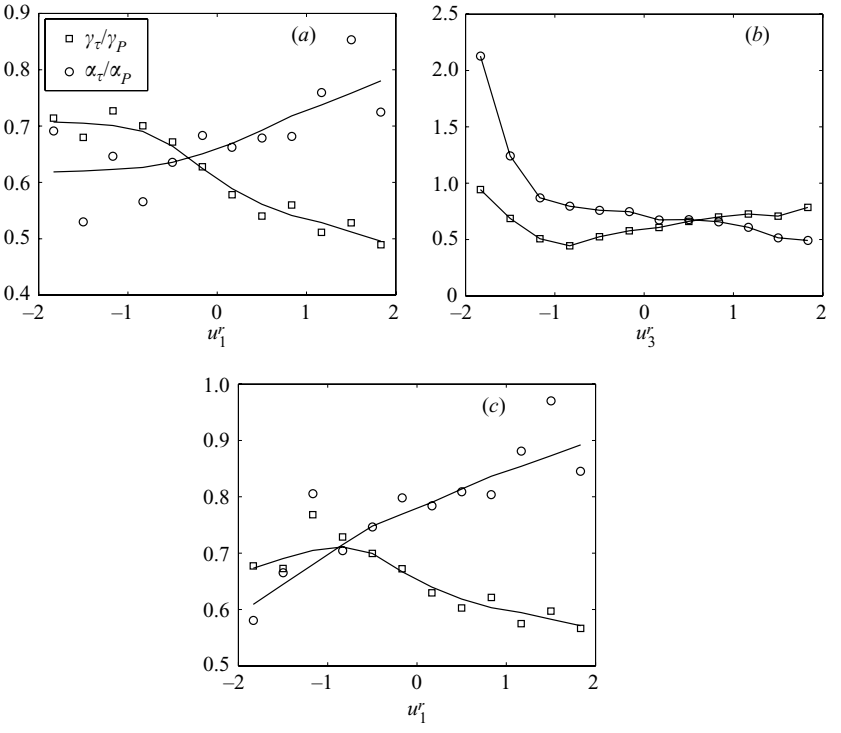

FIGURE 25. Ratios of the eigenvalues of the conditional SGS stress and the conditional SGS stress production conditional on (*a*) u_1^r and (*b*) u_3^r. The buoyancy production is included in (*c*).

is more anisotropic when both u_1^r and u_3^r are positive. The magnitude of α_β is generally small and weakly depends on u_1^r and u_3^r. In order to characterize the eigenvalue relationship between $\langle \tau_{ij}^d | \boldsymbol{u}^r \rangle$ and $\langle P_{ij}^a | \boldsymbol{u}^r \rangle$, we plot the ratio of α_τ/α_P and γ_τ/γ_P conditional on u_1^r and u_3^r in figures 25(*a*) and 25(*b*), respectively. The ratio of eigenvalue β_τ and β_P is not shown because both of them are small. The ratios α_τ/α_P and γ_τ/γ_P depend both on u_1^r and u_3^r, and the dependence on u_1^r is generally weaker than on u_3^r. The eigenvalue ratios of $\langle \tau_{ij}^d | \boldsymbol{u}^r \rangle$ and $\langle P_{ij}^a + A_{ij}^a | \boldsymbol{u}^r \rangle$ are also computed (not shown). The results are similar to those in figure 25(*a*, *b*) because the magnitude of the advection is small. The eigenvalue ratios of $\langle \tau_{ij}^d | \boldsymbol{u}^r \rangle$ and $\langle P_{ij}^a + P_{Bij}^a | \boldsymbol{u}^r \rangle$ conditional on u_1^r shown in figure 25(*c*) have larger variations than those in figure 25(*a*). The results of $\langle P_{ij}^a + P_{Bij}^a + A_{ij}^a | \boldsymbol{u}^r \rangle$ are close to the results of $\langle P_{ij}^a + P_{Bij}^a | \boldsymbol{u}^r \rangle$ (not shown).

The overall similarity between $\langle \tau_{ij}^d | \boldsymbol{u}^r \rangle$ and $\langle P_{ij}^a | \boldsymbol{u}^r \rangle$ can be quantified using their contraction,

$$\left\langle \tau_{ij}^d \middle| \boldsymbol{u}^r \right\rangle : \left\langle P_{ij}^a \middle| \boldsymbol{u}^r \right\rangle = \frac{\left\langle \tau_{ij}^d \middle| \boldsymbol{u}^r \right\rangle \left\langle P_{ij}^a \middle| \boldsymbol{u}^r \right\rangle}{\left| \left\langle \tau_{ij}^d \middle| \boldsymbol{u}^r \right\rangle \right| \left| \left\langle P_{ij}^a \middle| \boldsymbol{u}^r \right\rangle \right|}. \tag{6.3}$$

If the two tensors are perfectly aligned and their eigenvalues are proportional, the contraction has the value of one. The results in figure 26(*a*) show that the $\langle \tau_{ij}^d | u_1^r \rangle : \langle P_{ij}^a | u_1^r \rangle$ is close to one and weakly depend on u_1^r. The values in figure 26(*b*) are also close to one and weakly depend on u_3^r when u_3^r is positive, but decrease with increasing magnitude of u_3^r when u_3^r is negative. Again, for negative u_3^r, the eigenvalues of $\langle \tau_{ij}^d | u_3^r \rangle$ and $\langle P_{ij}^a | u_3^r \rangle$ are generally small and $\langle \tau_{ij}^d | u_3^r \rangle$ is less anisotropic, thus the alignment results are less well defined. The results also show that including the

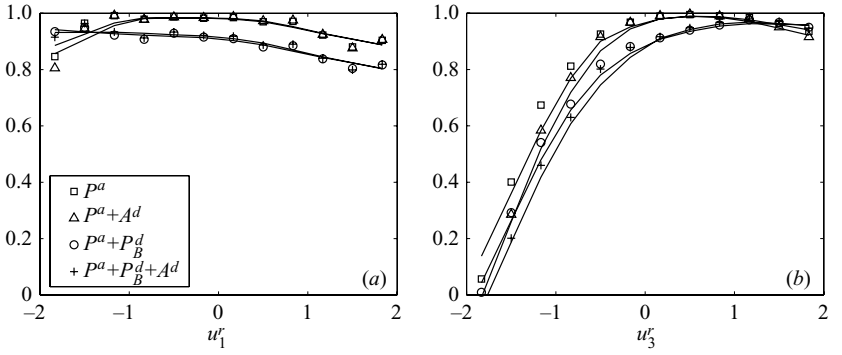

FIGURE 26. Contraction of the conditional SGS stress and the conditional SGS stress production conditional on (*a*) u_1^r and (*b*) u_3^r. The effects of advection and buoyancy production are also included and are generally small.

advection term has little effect on the contraction. However, including the buoyancy production rate causes the contraction to decrease and results in a stronger dependence on u_3^r. Therefore, in the presence of buoyancy, τ_{ij}^d/t_Δ is probably a better model for the sum of the pressure destruction, buoyancy production and advection. From a modelling point of view, because both $\langle \tau_{ij}^d | \boldsymbol{u}^r \rangle$ and $\langle P_{ij}^a | \boldsymbol{u}^r \rangle$ are small for negative u_3^r, it is probably more important to model correctly their magnitudes than orientations.

7. Conclusions

In the present study, we use field measurements data in the convective atmospheric boundary layer to analyse the subgrid-scale turbulence. The necessary conditions for LES to predict correctly the one-point resolvable-scale velocity JPDF are that the SGS model reproduces the conditional means of the SGS stress and the SGS stress production rate. The conditions highlight the importance of the conditional energy transfer from the resolvable to the subgrid scales and the production rate of SGS shear stress.

Analyses of the conditional SGS stress and the conditional SGS stress production using the field data show that they are closely related to the surface-layer dynamics. Specifically, the updrafts generated by buoyancy, the downdrafts associated with the large-scale convective eddies, the mean shear, and the length scale inhomogeneity play important roles in the behaviours of $\langle \tau_{ij} | \boldsymbol{u}^r \rangle$ and $\langle P_{ij} | \boldsymbol{u}^r \rangle$.

The results show that when u_3^r is positive (updrafts), the subgrid-scale eddies move upward and are on average stretched in the vertical direction owing to shear and buoyancy acceleration. Under such conditions, all three components of the normal SGS stress gain energy through the spectral transfer. However, τ_{33} loses energy to τ_{11} (and τ_{22}) through inter-component exchange, resulting in anisotropy in the SGS stress. These processes are enhanced with increasing u_3^r owing to stronger vertical shear and buoyancy acceleration as well as the advection effects. While $\langle P_{33} | u_1^r, u_3^r \rangle$ generally depends weakly on u_1^r, $\langle P_{11} | u_1^r, u_3^r \rangle$ depends on u_1^r, because a larger u_1^r causes stronger vertical shear, further increasing the level of anisotropy. For negative u_3^r, the subgrid-scale eddies associated with the returning flow of large convective eddies move downward and are on average compressed in the vertical direction owing to the presence of the ground. The spectral transfer is negative (conditional backscatter) under such conditions. However, τ_{33} gains energy from τ_{11} (and τ_{22}) through

inter-component exchange. These processes are also somewhat enhanced by increasing the magnitude of (negative) u_3^r, resulting in nearly isotropic SGS stress. These processes depend weakly on u_1^r because the vertical shear is weakened by the returning flow.

Representation of the conditional SGS stress in the Lumley triangle also shows similar trends for anisotropy. In general, the anisotropy is weak for negative u_3^r and is much stronger for positive u_3^r. For positive and negative u_1^r values, $\langle \tau_{ij} | u_1^r, u_3^r \rangle$ is close to axisymmetric with one large and one small eigenvalue, respectively, perhaps reflecting the shear and buoyancy effects. The results for the SGS shear stress $\langle \tau_{13} | u_1^r, u_3^r \rangle$ and the production term $\langle P_{13} | u_1^r, u_3^r \rangle$ are consistent with the dependence of the anisotropy on u_1^r and u_3^r. The magnitude of $\langle P_{13} | u_1^r, u_3^r \rangle$ depends on u_1^r and is enhanced by positive u_3^r. Comparisons of the results for different array configurations (Δ/z and $-z/L$) show that both grid anisotropy and the stability parameter ($-z/L$) affect the anisotropy of the SGS stress. The anisotropy of $\langle \tau_{ij} | \boldsymbol{u}^r \rangle$ is argued to be important for correctly predicting the mean velocity profile and the streamwise velocity variance. The results also show that there is significant similarity between $\langle \tau_{ij} | \boldsymbol{u}^r \rangle$ and $\langle P_{ij} | \boldsymbol{u}^r \rangle$ when u_3^r is positive. This is further evidenced by the small angles between their eigenvectors (less than 10°) and high values of the normalized tensor contraction (>0.9).

We perform systematic tests of several current SGS models. The Smagorinsky model can predict well neither the conditional mean of SGS stress nor its production. It can predict quite well the trends of some shear stress components, but not the normal components, and can predict the trends of some normal components of conditional SGS stress production, but not the shear components. The magnitudes of these components are generally poorly predicted. The level of anisotropy is also severely under-predicted.

The nonlinear model (Leonard 1974) can predict reasonably well the trends of some normal stress components, but not the shear components, and can predict the trends of some normal components and shear components of the conditional SGS stress production rate. It over-predicts the conditional backscatter. Unlike the Smagorinsky model, the nonlinear model over-predicts the level of anisotropy. The mixed Smagorinsky–nonlinear model does not show significant improvement. The deviatoric part of the mixed model has an improved performance. It can predict most components of the conditional SGS stress and the conditional SGS stress production quite well. Unfortunately, $\langle \tau_{13} | \boldsymbol{u}^r \rangle$ is poorly predicted, which is very important for LES in the surface layer. Although the anisotropy is over-predicted, it is closer to the measurements than the mixed model and the nonlinear model.

The predicted $\langle \tau_{13} | \boldsymbol{u}^r \rangle$ using Kosvić's nonlinear model is improved over of the deviatoric mixed model, but the rest of the components of the conditional SGS stress and the conditional SGS stress production are less well predicted. It also under-predicts the magnitude of the conditional SGS stress when the mean energy transfer is matched. The level of anisotropy is also under-predicted compared with measurements, but the prediction is improved over that of the Smagorinsky model.

Using the measured $\langle \tau_{ij} | \boldsymbol{u}^r \rangle$ and $\langle P_{ij} | \boldsymbol{u}^r \rangle$ and their model predictions, the deficiencies in current LES results, such as the over-predictions of the mean velocity profile and the streamwise velocity variance, and the under-prediction of the vertical velocity skewness are linked to the inability of the SGS models to predict $\langle \tau_{ij} | \boldsymbol{u}^r \rangle$ and $\langle P_{ij} | \boldsymbol{u}^r \rangle$ correctly. Specifically, the former is related to the under-prediction of the anisotropy of $\langle \tau_{ij} | \boldsymbol{u}^r \rangle$ and the latter is due to the under-prediction of the dependence of $\langle P_{33} | \boldsymbol{u}^r \rangle$ on u_3^r and the asymmetry in the dependence.

The analyses of the conditional SGS stress and the conditional SGS stress production rate can serve as an important guide in developing improved SGS models.

In particular, the understanding gained on the characteristics of the SGS stress and its production and the deficiencies identified of SGS models in predicting these characteristics can be used to improve specific aspects of LES results that are crucial to a given application. We emphasize that although the testing of the SGS models performed in the present study is *a priori* in nature, the linkage between the modelled terms and resolvable-scale velocity JPDF is strong because the analyses use the JPDF equation. Therefore, the test results can be used to identify the possible causes for LES deficiencies. Nonetheless, it would be very useful to carry out *a posteriori* testing of SGS models by comparing model predictions of $\langle \tau_{ij} | \boldsymbol{u}^r \rangle$ and $\langle P_{ij} | \boldsymbol{u}^r \rangle$ from actual LES with measurements.

We thank Drs Tom Horst, Don Lenschow, Chin-Hoh Moeng, Peter Sullivan and Jeff Weil at NCAR for conducting the field campaign of the HATS collaboration and for providing the data. We also thank Professor John C. Wyngaard for valuable discussions. This work was supported by the National Science Foundation through grant ATM-0222421.

REFERENCES

Adrian, R. J. 1990 Stochastic estimation of sub-grid scale motions. *Appl. Mech. Rev.* **43**, S214–S218.

Bardina, J., Ferziger, J. H. & Reynolds, W. C. 1980 Improved subgrid scale models for large-eddy simulation. *AIAA Paper* 80-1357.

Borue, V. & Orszag, S. 1998 Local energy flux and subgrid-scale statistics in three-dimensional turbulence. *J. Fluid Mech.* **366**, 1–31.

Cerutti, S., Meneveau, C. & Knio, O. M. 2000 Spectral and hyper eddy viscosity in high-Reynolds-number turbulence. *J. Fluid Mech.* **421**, 307–338.

Chen, Q., Zhang, H., Wang, D. & Tong, C. 2003 Subgrid-scale stress and its production rate: conditions for the resolvable-scale velocity probability density function. *J. Turbulence* **4**, 027.

Clark, R. A., Ferziger, J. H. & Reynolds, W. C. 1979 Evaluation of subgrid-models using an accurately simulated turbulent flow. *J. Fluid Mech.* **91**, 1–16.

Deardorff, J. W. 1970 A numerical study of three-dimensional turbulent channel flow at large Reynolds numbers. *J. Fluid Mech.* **41**, 453–480.

Deardorff, J. W. 1972 Numerical investigation of neutral and unstable planetary boundary layers. *J. Atmos. Sci.* **29**, 91–115.

Domaradzki, J. A., Liu, W. & Brachet, M. E. 1993 An analysis of subgrid-scale interactions in numerically simulated isotropic turbulence. *Phys. Fluids* A **5**, 1747–1759.

Edsall, R. M., Thomson, D. W., Wyngaard, J. C. & Peltier, L. J. 1995 A technique for measurement of resolvable-scale flux budgets. In *11th Symp. on Boundary Layers and Turbulence*, pp. 15–17. Am. Met. Soc. Charlotte, NC.

Germano, M., Piomelli, U., Moin, P. & Cabot, W. H. 1991 A dynamic subgrid-scale eddy viscosity model. *Phys. Fluids* A **3**, 1760–1765.

Gicquel, L. Y. M., Givi, P., Jaberi, F. A. & Pope, S. B. 2002 Velocity filtered density function for large eddy simulation of turbulent flows. *Phys. Fluids* **14**, 1196–1213.

Härtel, C., Kleiser, L., Unger, F. & Friedrich, R. 1994 Subgrid-scale energy-transfer in the near-wall region of turbulent flow. *Phys. Fluid* **6**, 3130–3143.

Horst, T. W., Kleissl, J., Lenschow, D. H., Meneveau, C., Moeng, C.-H., Parlange, M. B., Sullivan, P. P. & Weil, J. C. 2004 HATS: field observations to obtain spatially-filtered turbulence fields from transverse arrays of sonic anemometers in the atmosperic surface flux layer. *J. Atmos. Sci.* **61**, 1566–1581.

Jaberi, F. A., Miller, R. S. & Givi, P. 1996 Conditional statistics in turbulent scalar mixing and reaction. *AIChE J.* **42**, 1149–1152.

Juneja, A. & Brasseur, J. G. 1999 Characteristics of subgrid-resolved-scale dynamics in anisotropic turbulence, with application to rough-wall boundary layers. *Phys. Fluid* **11**, 3054–3068.

Kaimal, J. C., Wyngaard, J. C., Izumi, Y. & Coté, O. R. 1972 Spectral characteristic of surface-layer turbulence. *Q. J. R. Met. Soc.* **98**, 563–589.

Khanna, S. & Brasseur, J. G. 1997 Analysis of Monin–Obukhov similarity from large-eddy simulation. *J. Fluid Mech.* **345**, 251–286.

Kleissl, J., Meneveau, C. & Parlange, M. 2003 On the magnitude and variability of subgrid-scale eddy-diffusion coefficients in the atmospheric surface layer. *J. Atmos. Sci.* **60**, 2372–2388.

Kosović, B. 1997 Subgrid-scale modelling for the large-eddy simulation of high-Reynolds-number boundary layer. *J. Fluid Mech.* **336**, 151–182.

Langford, J. A. & Moser, R. D. 1999 Optimal LES formulations for isotropic turbulence. *J. Fluid Mech.* **398**, 321–346.

Leith, C. E. 1990 Stochastic backscatter in a subgrid-scale model: plane shear mixing layer. *Phys. Fluids* A **2**, 297–299.

Lemone, M. A. 1990 Some observations of vertical velocity skewness in the convective planetary boundary-layer. *J. Atmos. Sci.* **47**, 1163–1169.

Leonard, A. 1974 Energy cascade in large-eddy simulations of turbulent fluid flows. *Adv. Geophys.* **18**, 237–248.

Lesieur, M. & Métais, O. 1996 New trends in large eddy simulations of turbulence. *Annu. Rev. Fluid Mech.* **28**, 45–82.

Lilly, D. K. 1967 The representation of small-scale turbulence in numerical simulation experiments. In *Proc. IBM Scientific Computing Symp. Environ. Sci.* p. 195.

Liu, S., Katz, J. & Meneveau, C. 1999 Evolution and Modelling of subgrid scales during rapid straining of turbulence. *J. fluid Mech.* **387**, 281–320.

Liu, S., Meneveau, C. & Katz, J. 1994 On the properties of similarity subgrid-scale models as deduced from measurements in a turbulent jet. *J. Fluid Mech.* **275**, 83–119.

Lumley, J. L. 1965 Interpretation of time spectra measured in high-intensity shear flows. *Phys. Fluids* **6**, 1056–1062.

Lumley, J. L. 1978 Computational modelling of turbulent flows. *Adv. Appl. Mech.* **18**, 123–176.

Lund, T. S. & Novikov, E. A. 1992 Parametrization of subgrid-scale stress by the velocity gradient tensor. *Annual Res. Briefs – Center for Turbulence Res.* pp. 27–43.

McMillan, O. J. & Ferziger, J. H. 1979 Direct testing of subgrid-scale models. *Am. Inst. Aeronaut. Astronaut. J.* **17**, 1340–1346.

Mason, P. J. 1994 Large-eddy simulation: a critical review of the technique. *Q. J. R. Met. Soc.* **120**, 1–26.

Mason, P. J. & Thomson, D. J. 1992 Stochastic backscatter in large-eddy simulation of boundary layers. *J. Fluid. Mech.* **242**, 51–78.

Meneveau, C. 1994 Statistics of turbulence subgrid-scale stress: necessary conditions and experimental tests. *Phys. Fluids* **6**, 815.

Meneveau, C. & Katz, J. 2000 Scale-invariance and turbulence models for large-eddy simulation. *Annu. Rev. Fluid Mech.* **32**, 1–32.

Moeng, C.-H. 1984 Large-eddy simulation model for the study of planetary boundary-layer turbulence. *J. Atmos. Sci.* **41**, 2052–2062.

Moeng, C.-H. & Rotunno, R. 1990 Vertical-velocity skewness in the buoyancy-driven boundary-layer. *J. Atmos. Sci.* **47**, 1149–1162.

Moeng, C.-H. & Wyngaard, J. C. 1984 Statistics of conservative scalars in the convective boundary layer. *J. Atmos. Sci.* **41**, 3161–3169.

Nieuwstadt, F. T. M. & de Valk, P. J. P. M. M. 1987 A large eddy simulation of buoyant and non-buoyant plume dispersion in the atmospheric boundary layer. *Atmos. Environ.* **21**, 2573–2587.

Panofsky, H. A. & Dutton, J. 1984 *Atmospheric Turbulence*. Wiley-Interscience.

Peltier, L. J., Wyngaard, J. C., Khanna, S. & Brasseur, J. 1996 Spectra in the unstable surface layer. *J. Atmos. Sci.* **53**, 49–61.

Piomelli, U. 1993 High Reynolds-number calculations using the dynamic subgrid-scale stress model. *Phys. Fluid* A **5**, 1484–1490.

Piomelli, U., Moin, P. & Ferziger, J. H. 1988 Model consistency in large eddy simulation of turbulent channel flows. *Phys. Fluid* **31**, 1884–1891.

Piomelli, U., Yu, Y. & Adrian, R. J. 1996 Subgrid-scale energy transfer and near-wall turbulence structure. *Phys. Fluids* **8**, 215–224.

Pope, S. B. 1985 PDF methods for turbulent reacting flows. *Prog. Engng Combust. Sci.* **11**, 119–192.

Pope, S. B. 2000 *Turbulent Flows*. Cambridge University Press.

Pope, S. B. 2004 Ten questions concerning the large-eddy simulation of turbulent flows. *New J. Phys.* **6**, 1–24.

Porté-Agel, F., Meneveau, C. & Parlange, M. 2000 A scale-dependent dynamics model for large-eddy simulation: application to a neutral atmospheric buoyancy layer. *J. Fluid Mech.* **415**, 261–284.

Porté-Agel, F., Parlange, M. B., Meneveau, C. & Eichinger, W. E. 2001 A priori field study of the subgrid-scale heat fluxes and dissipation in the atmospheric surface layer. *J. Atmos. Sci.* **58**, 2673–2698.

Rajagopalan, A. G. & Tong, C. 2003 Experimental investigation of scalar–scalar-dissipation filtered joint density function and its transport equation. *Phys. Fluids* **15**, 227–244.

Rotta, J. C. 1951 Statistische theorie nichthomogener turbulenz. *Z. Phys.* **129**, 547–572.

Sabelnikov, V. A. 1998 Asymptotic solution of the equation for the probability distribution of a passive scalar in grid turbulence with a uniform mean scalar gradient. *Phys. Fluids* **10**, 753–755.

Sarghini, F., Piomelli, U. & Balaras, E. 1999 Scale-similar models for large-eddy simulations. *Phys. Fluids* **11**, 1596–1607.

Schmidt, H. & Schumann, U. 1989 Coherent structure of the convective boundary layer derived from large-eddy simulations. *J. Fluid Mech.* **200**, 511–562.

Schumann, U. 1975 Subgrid scale model for finite difference simulations of turbulent flows in plane channels and annuli. *J. Comput. Phys.* **18**, 376–404.

Shaw, R. & Schumann, U. 1992 Large-eddy simulation of turbulent flow above and within a forest. *Boundary-Layer Met.* **61**, 47–64.

Smagorinsky, J. 1963 General circulation experiments with the primitive equations: I. the basic equations. *Mon. Weather Rev.* **91**, 99–164.

Sullivan, P. P., Horst, T. W., Lenschow, D. H., Moeng, C.-H. & Weil, J. C. 2003 Structure of subfilter-scale fluxes in the atmospheric surface layer with application to large-eddy simulation modelling. *J. Fluid Mech.* **482**, 101–139.

Sullivan, P. P., McWilliams, J. C. & Moeng, C.-H. 1994 A subgrid-scale model for large-eddy simulation of planetary boundary-layer flows. *Boundary-Layer Met.* **71**, 247–276.

Tao, B., Katz, J. & Meneveau, C. 2000 Geometry and scale relationships in high Reynolds number turbulence determined from three-dimensional holographic velocimetry. *Phys. Fluids* **12**, 941–944.

Tong, C. 2001 Measurements of conserved scalar filtered density function in a turbulent jet. *Phys. Fluids* **13**, 2923–2937.

Tong, C. 2003 Galilean invariance of velocity probability density function transport equation. *Phys. Fluids* **15**, 2073–2076.

Tong, C., Wyngaard, J. C. & Brasseur, J. G. 1999 Experimental study of subgrid-scale stress in the atmospheric surface layer. *J. Atmos. Sci.* **56**, 2277–2292.

Tong, C., Wyngaard, J. C., Khanna, S. & Brasseur, J. G. 1997 Resolvable- and subgrid-scale measurement in the atmospheric surface layer. In *12th Symp. on Boundary Layers and Turbulence Vancouver, BC, Canada*, pp. 221–222. Am. Met. Soc.

Tong, C., Wyngaard, J. C., Khanna, S. & Brasseur, J. G. 1998 Resolvable- and subgrid-scale measurement in the atmospheric surface layer: technique and issues. *J. Atmos. Sci.* **55**, 3114–3126.

Vreman, B., Geurts, B. & Kuerten, H. 1997 Large-eddy simulation of the turbulent mixing layer. *J. Fluid Mech.* **339**, 357–390.

Wang, D. & Tong, C. 2002 Conditionally filtered scalar dissipation, scalar diffusion, and velocity in a turbulent jet. *Phys. Fluids* **14**, 2170–2185.

Wang, D., Tong, C. & Pope, S. B. 2004 Experimental study of velocity filtered joint density function and its transport equation. *Phys. Fluids* **16**, 3599–3613.

Wyngaard, J. C. 1992 Atmosperic turbulence. *Annu. Rev. Fluid Mech.* **24**, 205–233.

Wyngaard, J. C. 2004 Toward numerical modelling in the 'Terra Incognita'. *J. Atmos. Sci.* **61**, 1861–1826.

Wyngaard, J. C., Coté, O. R. & Izumi, Y. 1971 Local free convection, similarity, and the budgets of shear stress and heat flux. *J. Atmos. Sci.* **28**, 1171–1182.